ROYAL SOCIETY
OF CHEMISTRY

PAPER

Check for updates

Surface termination dependent carbon dioxide reduction reaction on Ti$_3$C$_2$ MXene†

Ling Meng, [ID] [ab] Li-Kai Yan, [ID] *[b] Francesc Viñes [ID] *[a] and Francesc Illas [ID] [a]

The use of two-dimensional (2D) MXene materials as highly efficient electrocatalysts for the carbon dioxide reduction reaction (CO$_2$RR) has gained considerable attention in the last few years. However, current computational studies on the CO$_2$RR are primarily focused on MXene materials with different types of metals or displaying fully −O or −OH terminated surfaces, which fail to account for the fact that as-synthesized MXenes possess mixtures of −O, −OH, −F, and/or −H surface groups. Here, a comprehensive density functional theory (DFT) study is carried out on the stability and impact of different surface terminations and moiety distributions on CO$_2$RR performance done on the prototype Ti$_3$C$_2$ MXene, analyzing the possible electrocatalytic synthesis of a series of CO$_2$RR products, from CO to H$_2$CO, HCOOH, CH$_3$OH, and CH$_4$ under favorable low pH and potential, U, reaction conditions, while considering the competitive H$_2$ evolution reaction (HER). From *ca.* 450 distinct surface terminations, four F-free models are selected as dominant in Pourbaix surface stability diagrams under low pH and U conditions, namely −OH, −OH$_{2/3}$O$_{1/3}$, −OH$_{1/2}$O$_{1/2}$, and −OH$_{1/3}$O$_{2/3}$, and one F-containing model, −F$_{1/3}$OH$_{1/3}$O$_{1/3}$. Results highlight the participation of surface −OH groups as H-donors, and the benefits of simultaneous hydrogenation from proton reduction and −OH H transfer. In addition, the presence of both −OH and −O groups is beneficial, reducing limiting potential, U_L, costs, as experimentally observed. On the −F$_{1/3}$OH$_{1/3}$O$_{1/3}$ model, the presence of −F is *per se* non-detrimental, moving the limiting step to an early stage and reducing the U_L. The overall results underscore the competitiveness of MXenes in the CO$_2$RR with respect to a Cu electrocatalyst reference, and the tunability possibilities to maximize the selectivity towards either the CO$_2$RR or the HER.

1. Introduction

With the steadily growing use of fossil fuels, carbon dioxide (CO$_2$) emissions have increased to a worrying exceedingly high level. One of the major issues facing nowadays society is climate change and the ultra-high energy prices, recently highlighted by the impressive European energy crisis in the winter of 2022.[1] Thus, the exploitation of new energy sources is crucial to avoid such energy constrains, where one very appealing way is to use carbon dioxide (CO$_2$) emissions as a C$_1$ chemical source, turning CO$_2$ economy into a waste-to-product model, and, by that, contributing to a carbon-neutral cycle.[2] For this, carbon reduction technologies are key, one of which is the use of electrocatalytic CO$_2$ reduction reaction (CO$_2$RR) to convert it into other useful chemicals and fuels. Most of these processes

imply hydrogenation reactions, and the full technology can be thought as green when powered by renewable energy sources, such as solar and wind power, and when the used hydrogen (H$_2$) is produced in the same way.[3–6]

So far, despite receiving widespread attention from both theoretical and experimental research communities,[7–9] the CO$_2$RR is yet not widely implemented on an industrial scale due to multiple reasons, main ones being its cost and the low reaction activity reached by present catalysts, implying that novel and/or costly materials are needed, often accompanied by slow reaction kinetics, which altogether increases the process price and efficiency.[10,11] In addition to the aforementioned factors, achieving high levels of selectivity, stability, and durability is still a critical challenge in the field of the CO$_2$RR.[12] Over the last few years, extensive research endeavours have been focused on countless catalysts, including both non-precious metal[13,14] and non-metal catalysts.[15,16] Among them, Cu-based heterogeneous catalysts have attracted much attention due to their ability to convert CO$_2$ to abundant multi-carbon products, such as hydrocarbons and alcohols, while being accessible in cost.[17,18] However, using these catalysts, the formation of methane (CH$_4$), the main component of biogas, still starts at potentials ranging from −0.9 V to −1.1 V *vs.* the reversible

aDepartament de Ciència de Materials i Química Física & Institut de Química Teòrica i Computacional (IQTCUB), Universitat de Barcelona, c/ Martí i Franquès 1-11, 08028, Barcelona, Spain. E-mail: francesc.vines@ub.edu

bInstitute of Functional Material Chemistry, Key Laboratory of Polyoxometalate Science of Ministry of Education, Faculty of Chemistry, Northeast Normal University, Changchun 130024, P. R. China. E-mail: yanlk924@nenu.edu.cn

hydrogen electrode (RHE).[19,20] In addition, their low reaction kinetics has been found to be influenced by limitations arising from linear scaling relations between reaction intermediate binding energies, translated in a restricted stability of adsorbed carbon monoxide (CO), *i.e.* CO*, and similar reaction intermediates such as CHO*, which eventually leads to a reduced activity.[21,22] Thus, the quest for new cost-effective CO_2RR catalysts with less negative potentials is still open.

In this context, MXenes, few-layered transition metal carbides and/or nitrides, have arisen as an attractive family of materials for the CO_2RR, given their superior conductivity and hydrophilicity, making them very promising catalysts for this purpose.[23] MXenes are two-dimensional (2D) materials with $M_{n+1}X_nT_x$ general chemical formula, where M denotes an early transition metal, X generally represents C and/or N, T_x denotes the surface functional group, intrinsic to the MXene synthesis procedure, and *n* normally ranges from 1 to 3,[24–26] although MXenes with $n = 4$ have been already reported.[27] MXenes are normally gained by selective etching from precursor MAX phases, where *A*, normally a *p*-element like Al or Si, is removed using a hydrofluoric acid (HF) solution,[28] although *in situ* HF can be used admixing lithium fluoride (LiF) with hydrochloric acid (HCl).[29] With these methods, a mixture of –O, –H, –OH, and –F of terminations is gained.[30,31] Still, the type and quantity of such terminations are highly sensitive to synthesis conditions such as etching time, temperature, or HF concentration.[32,33] For instance, high concentrations of HF lead to a larger number of –F terminations, while when lower HF concentrations are used more –O species are found.[31,34] On top of that, successful F-free synthesis protocols have been reported,[35] even cleaning protocols[36] or new synthetic routes[37] to acquire T_x-free MXenes and even tune the T_x with many other terminations. In short, all this casuistry can be used to design MXenes to suit specific applications, playing with composition, size, and surface termination.[38]

Focusing back on the CO_2RR, recently Li *et al.*[39] computationally screened bare M_3C_2 (groups IV, V, and VI) MXenes for the CO_2RR by density functional theory (DFT) means, predicting Cr_3C_2 and Mo_3C_2 as most promising candidates, with limiting potentials of −1.05 and −1.31 V to form CH_4. Handoko *et al.*[40] and Chen *et al.*[41] accounted for surface termination exploring –O and –OH moieties, respectively, finding that O-terminated MXenes can enhance the stability of reaction intermediates by coordinating hydrogen atoms, while OH-terminated MXenes display a high reactivity owing to the already presence of hydrogen atoms. As a result, the catalysts exhibited a lower overpotential and challenged the traditional scaling relationships, while simultaneously establishing new ones. Recently, Handoko *et al.*[42] also experimentally reported that the CO_2RR activity of Ti_2CT_x is related to the proportion of surface –F and –O moieties, in the sense that a higher amount of –F leads to a lower activity and selectivity. Note that C_2 coupling is also a current research focus, although the use of pure MXene is still a challenge, and most of the recent approaches dealt with defect engineering or heterostructures,[43,44] a common strategy to boost the CO_2RR to C_2,[45] like using Cu or Fe transition metal single atoms on $Ti_3C_2T_x$ or Mo_2C, respectively,[46,47] or dioxygen vacancies on $Mo_2TiC_2O_2$.[48] The focus here is on non-modified

MXenes, and, therefore, on C_1 products. Despite the numerous DFT investigations on bare or fully terminated MXenes, there is still a lack of analysis under realistic conditions, hindering the correlation between theoretical simulations and experimental results. Therefore, further comprehensive studies are required to finally elucidate and comprehend CO_2RR performance on MXenes.

This is tackled here taking the paradigmatic Ti_3C_2 MXene as a case study. This material, first synthesized in 2011,[49] is considered a MXene prototype, being the target of extensive research and development, and currently the most well-studied and mature MXene material.[50] Here we systematically analyze, by first-principles based calculations, the CO_2RR performance on Ti_3C_2 MXene with four different but realistic terminations in specific ranges of pH and potential, *U*, based on a surface stability assessment using computational Pourbaix diagrams[51,52] created by considering about 450 different surface terminations with different combinations of surface species.[53] By using these suited models, we gain valuable and detailed insights into the CO_2RR process under realistic working conditions, highlighting (i) the CO_2 activation capacity of the selected models considering the working temperature, *T*, and CO_2 partial pressure, p_{CO_2}, (ii) that the presence of –F species is unavoidable under acidic conditions when the MXene is extracted using fluorinated solvents, (iii) that, contrary to previous studies,[41,54,55] the fully –OH or –O terminated MXene models are challenged at less negative potentials, while MXene with mixed terminations would be more realistic CO_2RR electrocatalytic models under such conditions, with (iv) a new CO_2RR mechanism involving these termination groups in the hydrogenation steps, while (v) the presence of –F groups is found to be inherently not only non-detrimental, but to positively contribute when the surface coverage is limited, so that finally (vi) Ti_3C_2 with a stable ternary mixture containing –O and –OH groups with a small amount of –F exhibits one of the lowest bias-demanding CO_2RR, even if fully –OH terminated is, *a priori*, more selective, all in all showing that (vii) MXenes are, in general, improved electrocatalysts with respect to the usual Cu-electrocatalyst reference.

2. Theoretical aspects

2.1. Computational details

All the presented periodic DFT calculations were carried out using the Vienna *ab initio* simulation package (VASP).[56] The generalized gradient approximation (GGA) Perdew–Burke–Ernzerhof (PBE) exchange-correlation functional[57] was used, accurately suited in the description of MXenes energetics.[58–60] Additionally, Grimme's D3 approach was included to account for dispersive force interactions.[61] The core electron density and its impact on the valence electron density were described using the projector augmented wave (PAW) method developed by Blöchl,[62] as implemented by Kresse and Joubert.[63] Besides, the valence electron density was expanded on a plane wave basis set with a cutoff kinetic energy of 415 eV, high enough to acquire total energies converged below the chemical accuracy of 1 kcal $mol^{−1}$, *ca.* 0.04 eV,[64] the same order of accuracy obtained when

This journal is © The Royal Society of Chemistry 2024

J. Mater. Chem. A, 2024, **12**, 7856–7874 | **7857**

performing test calculations using an implicit solvent model[65] and thus found to be not required in the oncoming discussion.

Different supercell models were used in the construction of Pourbaix diagrams, in particular, $p(2\times2)$ and $p(3\times3)$ supercells of Ti_3C_2, where a full monolayer (ML) coverage is defined as having one surface moiety per each surface metal atom. The $p(2\times2)$ supercell was used to evaluate the pristine, fully –O, –OH, –H, and –F covered Ti_3C_2, as well as mixed cases with $\frac{1}{2}$ ML $vs.$ $\frac{1}{2}$ ML, $\frac{1}{4}$ $vs.$ $\frac{3}{4}$ of a ML binary coverage, and $\frac{1}{4}$, $\frac{1}{4}$, and $\frac{1}{2}$ of a ML ternary situation, while the $p(3\times3)$ supercell was employed to investigate binary situations with $\frac{1}{3}$ $vs.$ $\frac{2}{3}$ coverage, as well as ternary situations with an equal coverage of each component. For reaction mechanism evaluation, $p(3\times3)$ or $p(4\times4)$ supercells were used. A 20 Å vacuum was added to the slab models to ensure their appropriate isolation, while the Brillouin zone was sampled using an optimal $5\times5\times1$ **k**-point Γ-centered Monkhorst–Pack grid,[66] achieving as well the aforementioned chemical accuracy.

During the structural optimization, a convergence criterion of 10^{-5} eV was used for the electronic self-consistent field steps, while atomic positions were relaxed until forces acting on atoms were below 0.01 eVÅ^{-1}. Unless stated otherwise, all calculations were carried out spin polarized. The vibrational frequencies of the reaction surface species minima were determined by constructing and diagonalizing the Hessian matrix using finite differences of 0.03 Å in length to evaluate the analytical gradients,[67,68] yet only atomic displacements on the adsorbed species and terminations were considered, while substrate atoms were held fixed, $i.e.$ a decoupling of surface species with the material phonons was assumed.

2.2. Surface Pourbaix diagrams

The purpose of constructing a Pourbaix diagram in this study is to identify the most thermodynamically stable surface termination of the Ti_3C_2 MXene under the realistic working conditions of pH and U during the CO_2RR. Details can be found in previous work,[53] but still let us briefly explain the procedure here. Initially, a systematic sampling approach was employed to explore various high-symmetry adsorption sites for each studied termination, as illustrated in Fig. S1 of the ESI,† revealing that the H_{Ti} site was consistently the most favorable site for adsorption of any of the T_x surface terminations. This information was used to optimize and gain the free-energy of different surface terminations, either with single moieties, or with ratios in mixed situations, all as a function of the applied electrode potential, U, and pH, using to this end the computational hydrogen electrode (CHE) approach.[69] Note that diverse distributions of functional groups were accounted for, encompassing both highly regular and irregular arrangements. To account for the number of electrons (e^-), protons (H^+) and fluorine ions (F^-) involved during the adsorption processes, the stoichiometric coefficients $\nu(e^-)$, $\nu(H^+)$, and $\nu(F^-)$ were considered when constructing the reaction formation free energy equations required for the Pourbaix diagrams,[70] as;

$$\Delta G(\text{pH}, U) = \Delta G(0, 0) - \nu(H^+)k_BT \times \ln 10 \times \text{pH} - \nu(e^-)eU - \nu(F^-)eU_F,$$ (1)

where $\Delta G(0,0)$ is the formation energy of a given surface termination at zero pH and U, where U refers to the applied electrode potential $vs.$ the standard hydrogen electrode (SHE), e is the charge of an electron, and k_B is Boltzmann's constant. To account for the chemical potential of electron–proton pairs, we rely on the CHE model whereas the computational fluorine electrode (CFE) is used in the case of fluorine anions,[53] U_F being the reduction potential of fluorine, and the results for the different $p(2\times2)$ and $p(3\times3)$ supercells are comparable when normalizing by the surface area. By this, a Pourbaix diagram can be drawn showing, under any pH and U conditions, which surface termination exhibits the lowest ΔG, and that is shown here in Fig. S2 of the ESI,† either for F-containing situations, as expected from a MXene synthesized using HF,[71,72] or in the absence of fluorine ions, in case $Ti_3C_2T_x$ was obtained using a F-free synthesis method.[73]
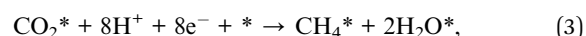
Ideally, for the CO_2RR, one would pursue situations with a minimal negative potential, and with low pH, in order to prompt the reaction kinetics. Thus, taking into account the potential working conditions of $T = 298.15$ K, $p_{H_2} = 1$ bar, pH < 4, and an improved applied potential U range of -0.75 V < U < 0 V, as commonly used in the CO_2RR towards CH_4 using MXene-based electrocatalysts,[39–42,74] the most suitable and realistic $Ti_3C_2T_x$ models were F-free $OH_{2/3}O_{1/3}$, $OH_{1/2}O_{1/2}$, $OH_{1/3}O_{2/3}$, and fully OH-terminated, as well as the F-containing $F_{1/3}OH_{1/3}O_{1/3}$, as illustrated in Fig. S2 of the ESI.† Already at this stage, one should notice how mixed situations are more the rule than the exception, and that fully OH-terminated models would be realistic only at low potentials, while O-terminated models would not be accurate situations for the CO_2RR. However, one must advert that most of the previous literature on MXenes focused on bare or fully O-terminated MXenes,[75,76] with only a limited number of studies considering –OH termination, and only Chen et $al.$[41] regarded the involvement of H atoms from the –OH termination in the CO_2RR.

2.3. CO_2RR mechanism

In general, the first step of CO_2 reduction is its adsorption from the gas phase, $CO_2^{(g)}$, on a catalyst free surface site (*);

$$CO_2^{(g)} + * \rightarrow CO_2*.$$ (2)

After this $sine$ qua non step, the rest of the reaction mechanism would imply proton-coupled electron transfer (PCET) steps, where protons, H^+, and electrons, e^-, are sequentially added. The full reduction of adsorbed CO_2 to adsorbed CH_4* and water (H_2O*) requires eight PCET electrochemical steps,[77] as:
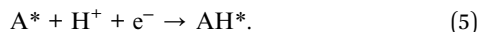
$$CO_2* + 8H^+ + 8e^- + * \rightarrow CH_4* + 2H_2O*,$$ (3)

followed by the subsequent desorption of CH_4* and H_2O* to the gas and liquid phases, respectively, as:

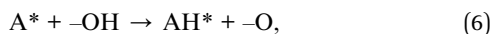$$CH_4* + 2H_2O* \rightarrow 2* + CH_4^{(g)} + 2H_2O_{(l)}.$$ (4)

For convenience, most of the earlier studies assumed that, for any precursor adsorbed species, A*, its reduction is done in

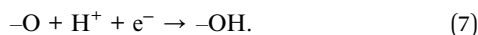a single elementary reaction, where one H^+ and one electron e^- are directly involved in producing AH*, as:

$$A* + H^+ + e^- \rightarrow AH*. \tag{5}$$

However, we here contemplated as well the possible involvement of termination –OH groups as a hydrogen source. Thus, for instance, in the presence of –OH surface moieties, the A* could be hydrogenated from the –OH group, as:

$$A* + \text{–OH} \rightarrow AH* + \text{–O}, \tag{6}$$

leaving behind an –O moiety in a chemical step. Later, an electrochemical step can be set up, where a proton is reduced on the as-formed –O moiety, regenerating the –OH group, as;

$$\text{–O} + H^+ + e^- \rightarrow \text{–OH}. \tag{7}$$

Notice as well that, thus, –O terminations could be reducing sites for medium H^+, which would act as a reservoir. According to this, one could elaborate an alternative path, where H^+ is reduced on a –O site, as in eqn (7), and in a later step, the as-formed –OH could be involved in the chemical hydrogenation of A* species, as in eqn (6). These different ordering pathways have been contemplated here, to gain a more complete understanding and involvement of surface terminations in the course of the CO$_2$RR and the followed mechanism.[53]

2.4. Thermodynamic approach

To outline the reaction mechanisms, a thermodynamic approach, as extendedly used in previous studies, has been used.[78,79] It implies that only the difference in Gibbs free energies between the different reaction intermediate states are relevant, and so used in determining the necessary limiting potential, U_L, for the reaction to take place. This succinctly implies that any PCET step features a latest transition state when endergonic, and an earliest transition state when exergonic, although a proportionality could be expected when the system under study follows the Brønsted–Evans–Polanyi (BEP) relationships.[80,81] Notice, still, that approaches are available to account for the transition states in the course of the reaction,[82,83] yet here, for comparative purposes with earlier studies,[84–86] they have not been accounted for.

The first step in outlining the reaction free energy profiles is to estimate the total adsorption energies of the intermediate species, ΔE_{ads}^i, so that

$$\Delta E_{ads}^i = E_{i/sub} - (E_{sub} + E_i). \tag{8}$$

Here, E_{sub} represents the energy of the substrate, here Ti$_3$C$_2$ MXene with the explored surface termination. E_i is the energy of the i adsorbed species as optimized in the vacuum, carried out at the Γ-point in a broken-symmetry box of $9 \times 10 \times 11$ Å^3 dimensions, to force the duly orbital occupancy. Lastly, $E_{i/sub}$ is the energy of the i moiety adsorbed on the specific studied substrate model. Thus, the more negative ΔE_{ads}^i is, the stronger is the adsorption.

When addressing the reaction ΔG calculations, one has to keep in mind that, by using the above-mentioned CHE reference,[69] under the standard equilibrium conditions of pH = 0, $U = 0$ V, a temperature T of 298.15 K, and a partial pressure of H$_2$, p_{H_2}, of 1 bar, the chemical potential of a pair of H^+ and e^- can be related to that of H$_2$ at 0 V $vs.$ the SHE, so that

$$H_{(aq)}^+ + e^- \rightarrow \tfrac{1}{2} H_2(g); \Delta G^\circ = 0 \text{ eV}, \tag{9}$$

where the chemical potentials or Gibbs free energies of the initial states, $H_{(aq)}^+ + e^-$, and the final state, $\tfrac{1}{2} H_2^{(g)}$, are identical. Note that, at variance with thermocatalysis, where T and p_{H_2} are normally used as variables of catalytic control, in electrocatalysis one normally works under the above standard conditions, while using pH and U_L as reaction variables, instead. Having this in mind, for any elementary reaction step, one can get the ΔG as

$$\Delta G = \Delta E + \Delta E_{ZPE} - T\Delta S, \tag{10}$$

which takes into account the reaction step energy difference, ΔE, the change in zero point energy (ZPE), ΔE_{ZPE}, and in entropy, ΔS. The ΔE term can be readily obtained from the total energies computed during the optimization, exemplified in eqn (5), as follows:

$$\Delta E = E_{AH*} - E_{A*} - \tfrac{1}{2} E_{H_2}. \tag{11}$$

Similarly, the ΔE_{ZPE} term can be gained as:

$$\Delta E_{ZPE} = E_{AH*}^{ZPE} - E_{A*}^{ZPE} - \frac{1}{2}E_{H_2}^{ZPE}, \tag{12}$$

where the ZPE term is gained from the computed vibrational frequencies, so that

$$E^{ZPE} = \frac{1}{2} \sum_{i=1}^{NMV} h\nu_i, \tag{13}$$

where ν_i represents the vibrational frequencies of the normal modes of vibration (NMV), and h Planck's constant. For a linear molecule in vacuum, the number of NMV is 3N-5 for a system with N atoms, while for any other type of molecule, the NMV is 3N-6. When adsorbed, any molecule or atom has 3N NMV, since free translations and rotations become restricted vibrational modes upon adsorption. Similarly, to ΔE_{ZPE}, the entropy change, ΔS, can be calculated as follows:

$$\Delta S = S_{AH*} - S_{A*} - \tfrac{1}{2}S_{H_2}. \tag{14}$$

The entropy of gas phase molecules has been obtained from the National Institute of Standards and Technology (NIST) webbook,[87] while for the adsorbed moieties, only the vibrational entropy (S_{vib}) is considered due to the ground state character and the hindrance of translations and rotations upon adsorption.[88] Thus, for adsorbed species, one has:

$$S = S_{vib} = k_B \sum_{i=1}^{NMV} \ln\left(1 - e^{-\frac{h\nu_i}{k_B T}}\right) - \sum_{i=1}^{NMV} h\nu_i \left(\frac{1}{e^{\frac{h\nu_i}{k_B T}} - 1}\right). \tag{15}$$

This journal is © The Royal Society of Chemistry 2024

J. Mater. Chem. A, 2024, **12**, 7856–7874 | **7859**

Given the reaction Gibbs free energy profiles, one can assess the reaction limiting potential, U_L, defined as the minimum potential required for a specific electrochemical reaction to occur spontaneously under given reaction conditions. In the case of the CO_2RR, U_L would be the potential at which each elementary electrochemical hydrogenation step becomes exergonic, indicating the minimum energy input required for the reaction to proceed. The descriptor ΔG_{max}, a free-energy model extracting the largest free-energy difference between intermediate states of an elementary step at a given target electrode potential, is used to quantify limiting potential for the CO_2RR, as

$$U_L = -\frac{\Delta G_{max}}{e},\qquad(16)$$

where, generally, the smaller the limiting potential, the higher the reaction activity.

2.5. Adsorption/desorption rates

Apart from the previous thermodynamic approach, it is worth keeping in mind that CO_2 adsorption must occur under the reaction conditions, while ideally a product such as CH_4 should desorb easily. This can be tackled here by profiling kinetic phase diagrams as used in the past.[89,90] In this approach, the molecule adsorption rate is compared to its desorption rate at different T and molecular partial pressures, finding turning points where adsorption and desorption rates are equal, i.e. equilibrium points. For the adsorption rate, r_{ads}, one can use non-activated collision theory,[91] such as:

$$r_{ads} = \frac{S_0 p_i A}{\sqrt{2\pi m_i k_B T}},\qquad(17)$$

where the initial sticking coefficient is denoted by S_0, p_i represents the partial pressure of the gas-phase molecule, either CO_2 or CH_4, and A represents the surface area of an adsorption site, established by dividing the supercell area of each surface by the number of possible sites, while m_i denotes the molecular mass. For the sticking coefficients, values of 0.4 and 0.01 were used for CO_2 and CH_4, respectively, as customary used in the past.[92,93]

To estimate the desorption rates, r_{des}, transition state theory (TST)[94] is used assuming that the desorbed transition state (TS) is a late two-dimensional (2D) TS. In this case, the energy barrier is given by the desorption energy, ΔE_{des}, which is simply the negative of the adsorption energy, ΔE_{des}, here without ZPE, as this term is already accounted for in the vibrational partition function, see below. Thus, r_{des} is defined as:

$$r_{des} = \nu_{des}\exp\left(\frac{\Delta E_{ads}}{k_B T}\right);\quad \nu_{des} = \frac{k_B T}{h}\frac{q_{trans,2D}^{gas}q_{rot}^{gas}q_{vib}^{gas}}{q_{vib}^{ads}},\qquad(18)$$

The ν_{des} prefactor is obtained from various partition functions, q, including $q_{trans,2D}^{gas}$, q_{rot}^{gas}, and q_{vib}^{gas}, which refer to the 2D translational, the rotational, and the vibrational partition functions, respectively, defined as

$$q_{trans,2D}^{gas} = A\frac{2\pi m k_B T}{h^2},\qquad(19)$$

$$q_{vib}^{ads/gas} = \prod_i \frac{\exp\left(-\dfrac{h\nu_i}{2k_B T}\right)}{1 - \exp\left(-\dfrac{h\nu_i}{k_B T}\right)},\qquad(20)$$

$$q_{rot}^{gas} = \frac{T}{\sigma^{sym}T_{rot}},\qquad(21)$$

where σ^{sym} is the molecular symmetry number, 2 and 12 for CO_2 and CH_4, respectively,[89,95] and T_{rot} the rotational temperature, 0.561 and 122 K for CO_2 and CH_4, respectively.[96,97] Note that the vibrational partition function of the adsorbed state, q_{vib}^{ads}, takes into account the frustrated rotations and translations as discussed above.

3. Results and discussion

3.1. MXene models, CO_2 activation, and CH_4 physisorption

The CO_2RR species have been optimized on the five considered surface-terminated $Ti_3C_2T_x$ models as depicted in Fig. 1, in turn derived from Pourbaix diagrams shown in Fig. S2 of the ESI.† Notice that according to their density of states (DOS) and projected DOS (PDOS), all models exhibit a metallic character, and generally with a large number of states at the Fermi energy, see Fig. S3 of the ESI,† which is a prerequisite for electrocatalysis, cf. ref. 47. One of the first aspects to tackle is whether CO_2 is attached and activated on such terminations. According to Le Sabatier principle,[98] CO_2 should moderately adsorb, enough to remain not strongly bound to prevent catalyst poisoning, yet not weakly enough to enable sufficient opportunities for its chemical bond breaking.[99] On the other hand, a product such as CH_4 should also moderately adsorb, enough to permit its release, and, more importantly, not too strongly, to avoid the self-poisoning of the electrocatalyst by the methane product.

In order to investigate the interaction between CO_2 and the chosen surface-terminated $Ti_3C_2T_x$ models, various adsorption sites were examined in a systematic fashion, taking into account the interaction with respect to different surface moieties (cf. Fig. S4a of the ESI†) and CO_2 orientations (cf. Fig. S4b of the ESI†), including vertical orientations, but also planar situations with different molecular orientations. This systematic procedure, here exemplified on CO_2, has been carried out for the rest of the reaction species and intermediates, with energy minima structures duly characterized by frequency analysis. The adsorptive configurations are shown in Fig. 2, and comparative adsorption energies in Fig. 3. As can be seen, generally CO_2 keeps its linear geometry on any explored surface termination, except for the full –OH termination, where the molecule has an E_{ads} of −0.71 eV, gets bent by 135.9°, negatively charged by 0.80 e, and with a mean bond elongation of C–O bonds by 1.25 Å, in full accordance with CO_2 being activated.[100,101] Clearly, the presence of surface –O groups is detrimental to activating CO_2, and only on fully –OH terminated MXene, the negatively charged CO_2, with charge mostly present on its O atoms, is stabilized with the slightly positively charged H atoms of surface –OH groups, see Fig. 2, with Bader charges of −0.73e, and it is also observed with the –OH group H charge depletion shown in
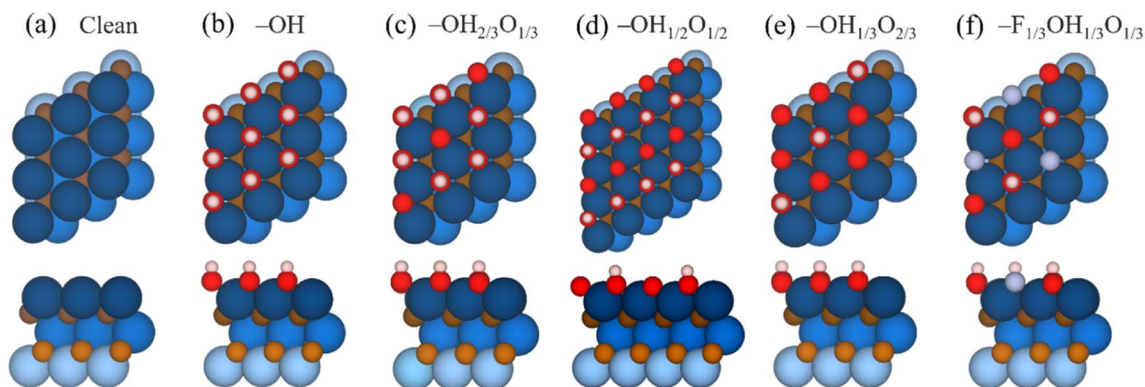
7860 | J. Mater. Chem. A, 2024, 12, 7856–7874

This journal is © The Royal Society of Chemistry 2024

Fig. 1 Top (upper images) and side (lower images) views of the $p(3\times3)$ Ti_3C_2 MXene (0001) surface with (a) a clean surface, (b) full $-OH$, (c) $-OH_{2/3}O_{1/3}$, (d) $-OH_{1/2}O_{1/2}$. here of $p(4\times4)$ supercell, (e) $-OH_{1/3}O_{2/3}$, and (f) $-F_{1/3}OH_{1/3}O_{1/3}$ terminations. Termination H, O, and F atoms are represented by white, red, and light lilac spheres, respectively, while Ti and C atoms are shown as blue and brown spheres, with different levels of shading depending on their stacking position, with darker versions being closer to the shown surface.
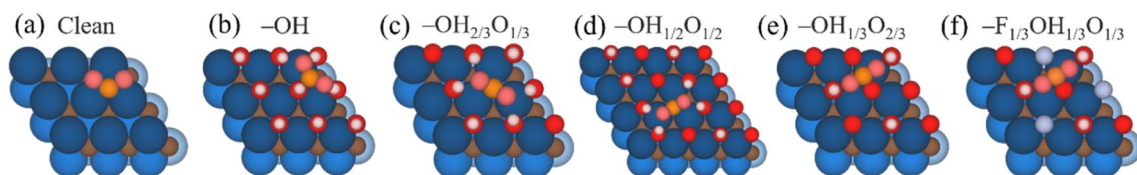

Fig. 2 Top views of optimal CO_2 adsorption sites on the Ti_3C_2 MXene model (0001) surface with (a) a clean surface, (b) full $-OH$, (c) $-OH_{2/3}O_{1/3}$, (d) $-OH_{1/2}O_{1/2}$, (e) $-OH_{1/3}O_{2/3}$, and (f) $-F_{1/3}OH_{1/3}O_{1/3}$ terminations. Colour coding as in Fig. 1, with CO_2 C and O atoms shown as orange and pink spheres, respectively.
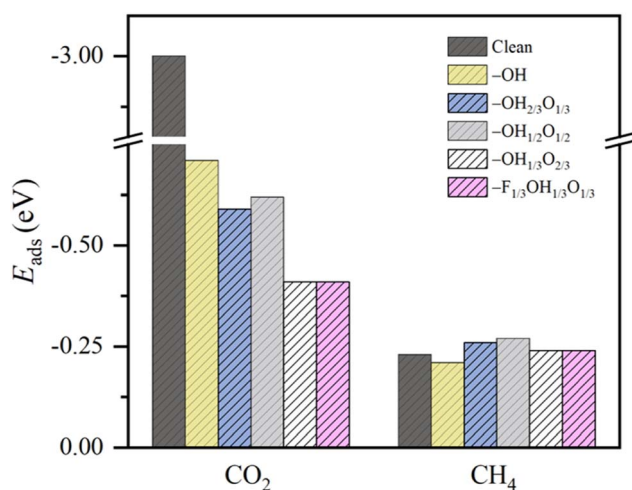

Fig. 3 Adsorption energies of CO_2 and CH_4, ΔE_{ads}, on the studied $Ti_3C_2T_x$ MXene (0001) surface models with a clean surface, full $-OH$, $-OH_{2/3}O_{1/3}$, $-OH_{1/2}O_{1/2}$, $-OH_{1/3}O_{2/3}$, and $-F_{1/3}OH_{1/3}O_{1/3}$ terminations. All values are given in eV.

the charge density difference (CDD) plots, see Fig. S5 of the ESI.†,[53]

This behavior contrasts with, *e.g.* CH_4 adsorption energies, see Fig. 3, where methane is physisorbed in any surface model, with E_{ads} ranging -0.21 to -0.27 eV. Here, actually, the presence of $-O$ groups is slightly beneficial, allegedly forming H

bonds with those of CH_4. Curiously, the stronger affinity towards CO_2 compared to CH_4 is in line with previous reports on pristine, surface termination free MXenes, as reported in the literature,[102] where such values were used to estimate CO_2 and CH_4 adsorption and desorption rates in the context of biogas upgrading. Note that the adsorption energies for both CO_2 and CH_4 are coincidental on $-OH_{1/3}O_{2/3}$ and $-F_{1/3}OH_{1/3}O_{1/3}$ models, since they belong to very similar local environments. Analogously, we estimated such adsorption/desorption rates as explained above, see Fig. S6 of the ESI,† in order to generate the so-called kinetic phase diagrams, present in Fig. 4.

Briefly, there, depending on the working conditions of temperature, T, and gases pressure, p, one can estimate the preference of the surfaces in adsorbing (or desorbing) such species. From them, it is evident that, *e.g.*, working at 300 K and 1 bar pressure, all surface models are favourable for attaching the CO_2 reactant, a premise of the reaction that is met. Moreover, the release of the eventual CH_4 product would be favoured in any explored model even in an atmosphere of 1 bar of CH_4, according to the kinetic phase diagrams of Fig. 4, a sought-after feature of a working electrocatalyst which underlies that no CH_4 self-poisoning is envisaged on such MXene models. From all the surface-terminated studied models, the fully $-OH$ terminated model exhibits the strongest CO_2 adsorption and CH_4 desorption capabilities, while, as the surface concentration of $-OH$ moiety decreases, these differences gradually diminish. Furthermore, when $-F$ is present, as in $-F_{1/3}OH_{1/3}O_{1/3}$, similar

This journal is © The Royal Society of Chemistry 2024
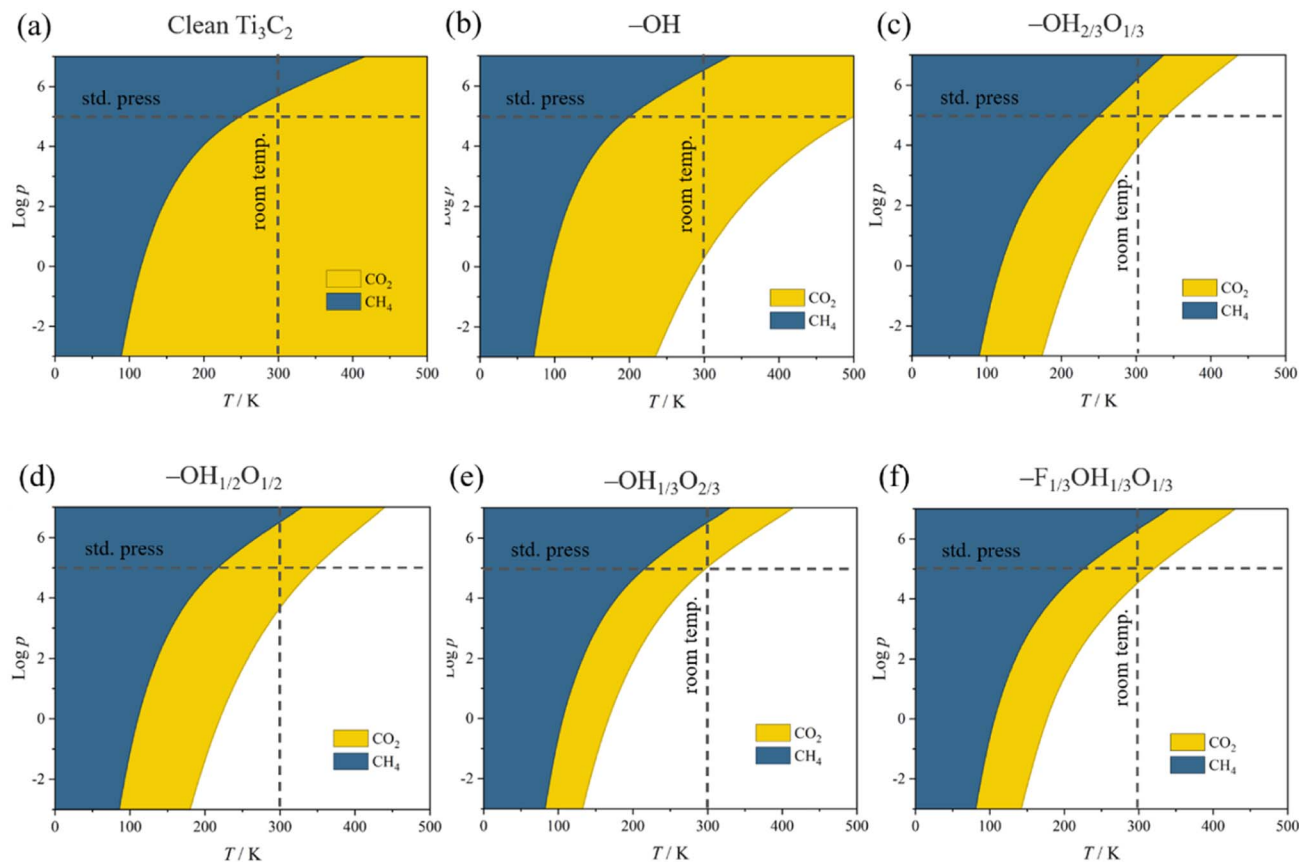
J. Mater. Chem. A, 2024, **12**, 7856–7874 | **7861**

Fig. 4 Calculated adsorptive kinetic phase diagrams for CO_2 and CH_4 on (a) a clean surface, (b) full $-OH$, (c) $-OH_{2/3}O_{1/3}$, (d) $-OH_{1/2}O_{1/2}$, (e) $-OH_{1/3}O_{2/3}$, and (f) $-F_{1/3}OH_{1/3}O_{1/3}$ terminations as a function of the logarithm of gas pressures, p, in Pa. Coloured regions imply preference towards adsorption, while colourless areas represent regions where one would expect surfaces to be free of such molecules.

kinetic phase diagrams are gained compared to $-OH_{2/3}O_{1/3}$, implying, to some extent, a similar role of both $-OH$ and $-F$ groups, with similar charges of $ca.$ -1 e, and comparable electric fields.

3.2. CO_2RR electrocatalysis mechanisms

After having established the suited surface-terminated MXene models for CO_2RR conditions, and the CO_2 and CH_4 adsorptive/desorptive conditions, the electrocatalytic performance is put under the inspection light, depicting the Gibbs free energy landscapes under standard working conditions, $T = 298.15$ K, $p_{H_2} = 1$ bar, pH $= 0$, and $U = 0$ V, to extract from them the limiting potential, U_L, as the main indicator of the electrocatalytic performance, yet the H-vacancy energetic cost, $E_{H_{vac}}$, is also used here to discuss the ease of T_x trapping H adatoms from surface $-OH$ groups, defined as

$$E_{H_{vac}} = E_{T_x\text{-}H} + \frac{1}{2}E_{H_2} - E_{T_x}, \qquad (22)$$

where $E_{T_x\text{-}H}$ describes the energy of MXene with a H-containing T_x termination, but with one missing H-atom, $\frac{1}{2}E_{H_2}$ accounts for the formation of a single H atom, released as half a H_2 molecule, and E_{T_x} is the energy of the H-containing T_x-terminated MXene. Within this definition, the more negative $E_{H_{vac}}$ is, the

weaker H binds to the MXene surface, and so the easier is its transfer.

Let us begin the analysis with the highly active $-OH$ surface termination, as observed with the high affinity towards CO_2, see Fig. 4. This affinity prompts the formation of stable HCO_2^* during the CO_2 adsorption involving a H atom from a surface $-OH$ group, being more stable by 2.22 eV, see Fig. 5, and energetically preferred over the direct electrochemical hydrogenation of CO_2 over an otherwise untouched $-OH$ surface termination. It is mandatory here to note that the H transfer from the $-OH$ group is spontaneous, and not artificial, neither in the $-OH$ surface termination nor in the other models, as several attempts were made to prevent it. Thus, it is apparent that the resulting moiety is quite stable, and that drives the H transfer from neighboring $-OH$ due to their proximity. Once HCO_2^* is formed in a chemical step, the attention is driven towards the first PCET electrochemical step, finding that hydrogenation at the C atom is most favorable, H_2CO hydrogenation at the O atom implies at least a ΔG of 1.89 eV, yet stabilizing the system by only 0.04 eV. This step spontaneously draws two more surface H atoms from two vicinal $-OH$ groups, forming a $H_2C(OH)_2$ compound, $i.e.$ methanediol or methylene glycol. In the second PCET, the involvement of one $-OH$ in the methylene glycol synthesis is then reverted so that
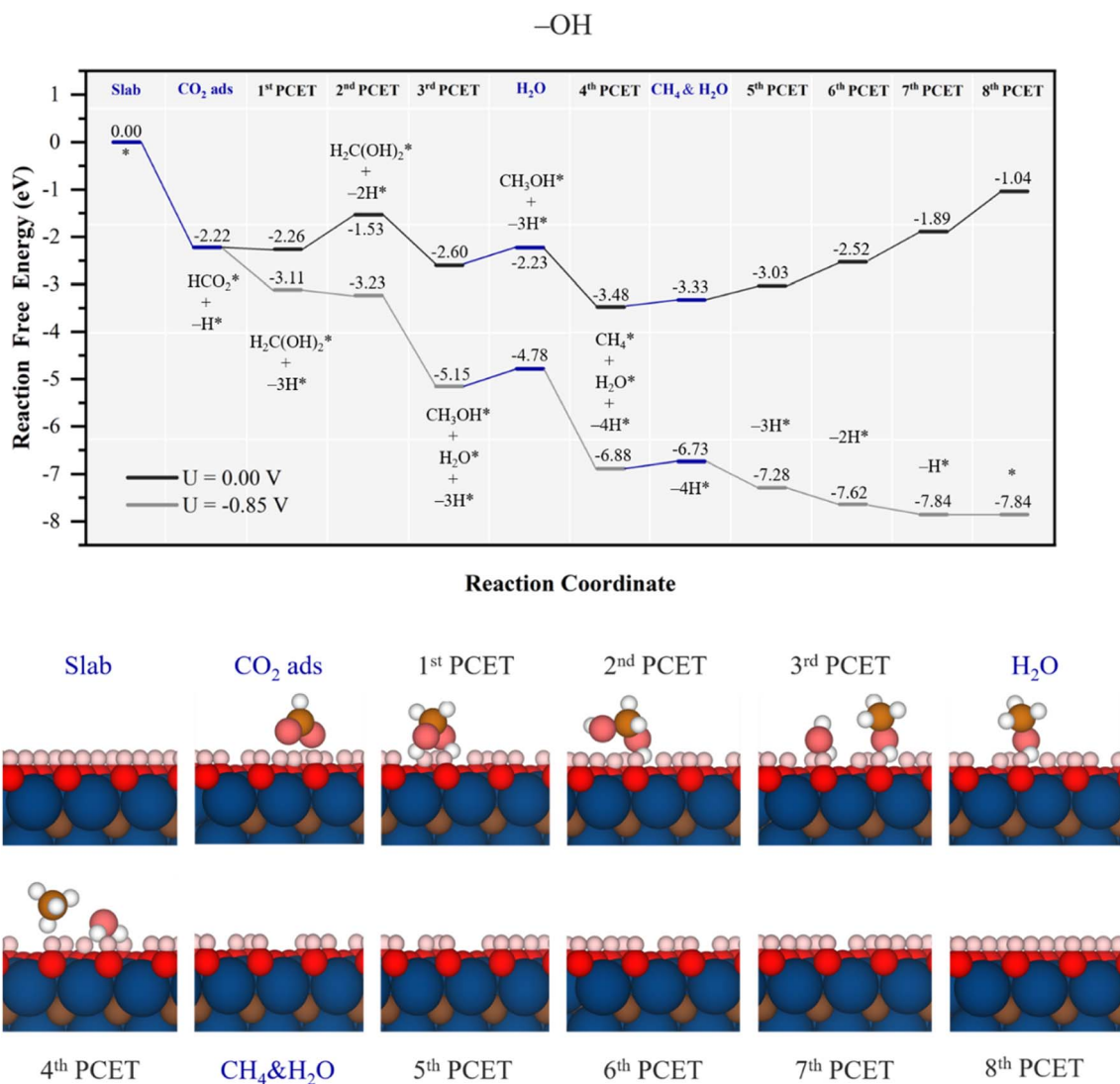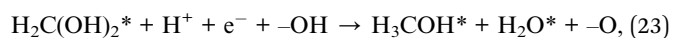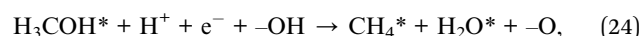
7862 | J. Mater. Chem. A, 2024, 12, 7856–7874

This journal is © The Royal Society of Chemistry 2024

Fig. 5 Gibbs free energy, ΔG, diagram of the CO_2RR on fully –OH terminated Ti_3C_2 MXene, under standard working conditions. Blue lines represent chemical steps of as-generated H_2O or CH_4 desorption, or CO_2 adsorption, while black and grey lines represent the electrochemical proton-coupled electron transfer (PCET) steps under zero and applied $U = U_L$ calculated potential of -0.85 V vs. SHE, respectively. The nH^* symbols refer to how many H atoms have been transferred from surface –OH groups at the reaction stage. Bottom panels show side views of atomic structures of different reaction stages. Colour coding as in Fig. 2.

hydrogenation of the as-formed surface –O group back to –OH proceeds with a ΔG of 0.73 eV.

Still, the regenerated –OH is able to again participate in the course of the reaction, along with the third PCET, forming methanol and water, i.e.

$$H_2C(OH)_2^* + H^+ + e^- + -OH \rightarrow H_3COH^* + H_2O^* + -O, \quad (23)$$

a quite favorable reaction step with a ΔG of -1.07 eV, and so thermodynamically preferred over the methylene glycol desorption. After this, the as-formed water can desorb, requiring 0.37 eV. Finally, in the fourth PCET, a similar situation occurs, where the reduced proton combines with a hydrogen from a surface –OH group, to form methane and water, as

$$H_3COH^* + H^+ + e^- + -OH \rightarrow CH_4^* + H_2O^* + -O, \quad (24)$$

with a noticeable ΔG of -1.25 eV, and preferred over the methanol desorption, requiring 0.71 eV, see Fig. S7 of the ESI.† At this point of the reaction, four PCET electrochemical steps have occurred, while four surface –OH groups have been consumed, supplying the remaining four PCET for the full methanation of CO_2. After CH_4 and H_2O desorption, requiring solely 0.15 eV, the remaining PCET steps are involved in regenerating the consumed surface –OH groups, with the subsequent ΔG values of 0.45, 0.51, 0.63, and 0.85 eV, respectively.

Notice here how energetically influential is the cooperative and simultaneous hydrogenation from solution protons and surface –OH groups, quite reducing the methylene glycol,
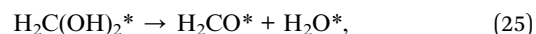
This journal is © The Royal Society of Chemistry 2024

J. Mater. Chem. A, 2024, **12**, 7856–7874 | **7863**

methanol, and methane formation steps. This mechanism occurs thanks to the low $E_{H_{vac}}$ of the –OH surface termination, with a value of -0.56 eV, see Table 1, implying that such surface H atoms are relatively easy to capture and thus to participate in the reaction, and underscores the exceptionally high participation of the H atoms from the –OH groups, to the point that molecular synthesis is not the potential determining step (PDS), but the electrocatalyst surface regeneration, with a ΔG_{max} of 0.85 eV. The corresponding theoretical limiting potential U_L is -0.85 V $vs.$ RHE, as depicted in Fig. 5, in which each electrochemical step is exergonic, while the chemical steps demand, at most, 0.37 eV for water release, feasible under working conditions. In addition, the U_L falls well within the stability region of the –OH model on the Pourbaix diagram in Fig. S2 of the ESI† at low pH, consistently implying the stability and recovery of the –OH terminated Ti_3C_2 electrocatalyst.

Furthermore, the selectivity of the catalyst is also, a $priori$, remarkable. As can be seen in alternative reaction paths shown in Fig. S7 of the ESI,† the two-electron synthesis of formic acid, $HCOOH_{(l)}$, is quite hindered by the formation of HCOOH* from HCO_2*, requiring 1.88 eV, while four-electron synthesis of formaldehyde, CH_2O*, from methylene glycol is disfavoured by 0.88 eV. Apart from these possible products, CO formation is avoided given the high stability of HCO_2* and the downhill formation of methylene glycol thanks to the participation of surface –OH groups transferring H atoms. Similarly, methanol synthesis is also quite hindered by the quite downhill formation of methane and water, see Fig. 5 and S7 of the ESI.† Thus, apart from the competitive hydrogen evolution reaction (HER), with an estimated U_L of -0.48 V using the very same computational scheme,[53] the synthesis of CH_4 competes with that of CH_2O in a similar fashion on fully –OH terminated Ti_3C_2 MXene, and only formic acid would be obtained at a very low potential of -1.88 V.

When –OH groups are partially replaced by –O, as in the –$OH_{2/3}O_{1/3}$ model, a different scenario unfolds, as illustrated in Fig. 6. In contrast to the full –OH coverage case, the reduced availability of surface H atoms, in line with a positive value of $E_{H_{vac}}$ of 0.12 eV, see Table 1, hampers the CO_2 molecule ability to capture surface H atoms before the electrochemical steps start, and so diminishes the involvement of surface H atoms in the oncoming PCET steps. Thus, CO_2 adsorption is mild, of -0.16 eV, and the initial formation of HCO_2* occurs by a PCET,

with a ΔG of -0.35 eV, whereas the possible step related to surface H atom leading to adsorbed formic acid, HCOOH*, is disadvantageous by 0.21 eV, see Fig. S8 of the ESI.† From HCO_2*, the formation of methylene glycol is fostered by a PCET step coupled with two surface H transfers, being an uphill process of 0.71 eV, see Fig. 6, but still more favorable than formic acid formation by a second PCET, with a ΔG of 0.92 eV, see Fig. S8 of the ESI.† However, in the subsequent step, *HCO_2 captures a total of two surface H atoms, which play a crucial role in the second PCET to form methylene glycol. Here, the third PCET is similar to that occurring on the fully –OH covered model, with regeneration of a surface –OH group after methylene glycol formation, here downhill by 0.3 eV, while following regeneration is uphill by 0.24 eV.

However, from the 5th PCET on, there is a notable shift of –O termination activity, with a higher propensity for proton reduction. Thus, this reduction has a ΔG of 0.61 eV, and preferred by 0.12 eV over the proton-reduction induced methylene glycol decomposition into formaldehyde and water, see Fig. S8 of the ESI,† as:

$$H_2C(OH)_2* \rightarrow H_2CO* + H_2O*, \quad (25)$$

an uphill process maintained in the 6th PCET with a ΔG of 0.76 eV. Actually, on this bifurcation, the system is much more favourable for methanol formation, as in eqn (23), a quite exergonic electrochemical step with a ΔG of -1.18 eV. After the as-formed H_2O is released, requiring 0.34 eV, the CH_3OH* can either desorb requiring 0.56 eV or get a vicinal reduced H, slightly less energy demanding by 0.06 eV. However, when this last electrochemical step occurs, eqn (24) is triggered, with a ΔG of -1.52 eV. Thus, under this picture, the methane formation PDS is this last CH_3OH* + H* adduct formation, with a ΔG value of 0.84 eV, and a resulting U_L of -0.84 V $vs.$ SHE, and so, similar to full –OH termination. Actually, the required U_L falls within the full –OH model stability according to the F-free Pourbaix diagram in Fig. S2 of the ESI† under acidic conditions, and would be viable only at neutral pH, although it is widely recognized that the electrocatalytic activity in more alkaline media is generally lower compared to acidic conditions.[103] Even if here the U_L is similar to that for the model with full –OH coverage, the PDS also corresponds to a late electrochemical stage, the CH_3OH* + H* adduct formation, instead of –OH regeneration, and the mechanisms present similarities, including methylene glycol formation and decomposition, and methanol decomposition. The main difference between both models is the involvement of both –OH and –O groups, as H donors and acceptors, respectively. The –OH may be regarded as a H reservoir, through a Volmer step, and also as a donor, thus having a dual functionality. As per the selectivity, the chemistry involved in the –$OH_{2/3}O_{1/3}$ model appears to be less selective than that of the fully –OH terminated, since channels leading to formic acid exist, with a U_L of solely -0.21 V, -0.71 V for methylene glycol, and -0.73 V for $CH_2O_{(l)}$, and with a similar production of methanol and methane according to the competitive desorption of as-formed CH_3OH and its reaction to generate methane, see Fig. 6 and S8 of the ESI,† with no route

Table 1 Summary of the PCET PDS as well as specific electrochemical reaction step, on the explored surface-terminated Ti_3C_2 models, under CO_2RR working conditions. The required U_L in V, and surface $E_{H_{vac}}$ in eV, values are specified

Model	PCET	PDS	$E_{H_{vac}}$	U_L
–OH	8th	$-H* \rightarrow *$	-0.56	-0.85
–$OH_{2/3}O_{1/3}$	7th	$CH_3OH* + * \rightarrow CH_3OH* + H*$	0.12	-0.84
–$OH_{1/2}O_{1/2}$	6th	$CH_3OH* + -H* \rightarrow CH_3OH* + *$	0.26	-0.70
–$OH_{1/3}O_{2/3}$	1st	$CO_2* \rightarrow HCOOH* + -H*$	0.73	-0.37
–$F_{1/3}OH_{1/3}O_{1/3}$	2nd	$HCOOH* + -H* \rightarrow HCOOH* + *$	0.31	-0.51

towards the CO formation. In addition, with such a model, the reported HER U_L is only of -0.08 V,[53] so, if any, such MXene termination would be better advisable to synthesize formic acid given the suited potential, matching the Pourbaix diagram stability shown in Fig. S2 of the ESI,† but with a competition to $H_2^{(g)}$ generation through the HER.

When further increasing the $-O/-OH$ ratio as in the $-OH_{1/2}O_{1/2}$ model, again some similitudes with respect to the profile on the $-OH_{2/3}O_{1/3}$ model are kept, see Fig. 6 and 7, also in line with a similar degree of H transfer, with an $E_{H_{vac}}$ of 0.26 eV, see Table 1, similar to the value of 0.12 eV for the $-OH_{2/3}O_{1/3}$ model. Again, the reaction starts with CO_2 physisorption with an E_{ads} of -0.06 eV only, but now, given the extra room to accommodate formic acid, the 1st PCET is coupled with an $-OH$ group H transfer leading to HCOOH*, which is exergonic by -0.3 eV, see Fig. 7. However, this formic acid is strongly adsorbed by 1.08 eV, see Fig. S9 of the ESI,† thus preventing its release.

Consequently, the reaction advances through a 2nd PCET forming formate with a ΔG of -0.17 eV, *i.e.* transferring one H back to the substrate, thus reducing a nearby $-O$ group, underscoring that formate stability is quite related to the presence of nearby $-O$ groups.

After formate is synthesized, a 3rd PCET involves again H transfer from two nearby $-OH$ groups and one proton reduction, to again lead to the adsorbed methylene glycol moiety, with an energy cost of 0.41 eV, followed once more by on surface $-O$ group reduction, costly only by 0.15 eV. Similarly to the model with $-OH_{2/3}O_{1/3}$ surface terminations, the rest of the reaction follows a similar pathway; the methylene glycol decomposition, as induced by a proton reduction coupled to a surface $-OH$ hydrogen transfer results in CH_3OH* and H_2O* in a quite exergonic electrochemical step with a ΔG of -0.77 eV, much more preferred than, *e.g.* decomposition towards formaldehyde, endergonic by 0.46 eV. After water desorption, methanol competes in between
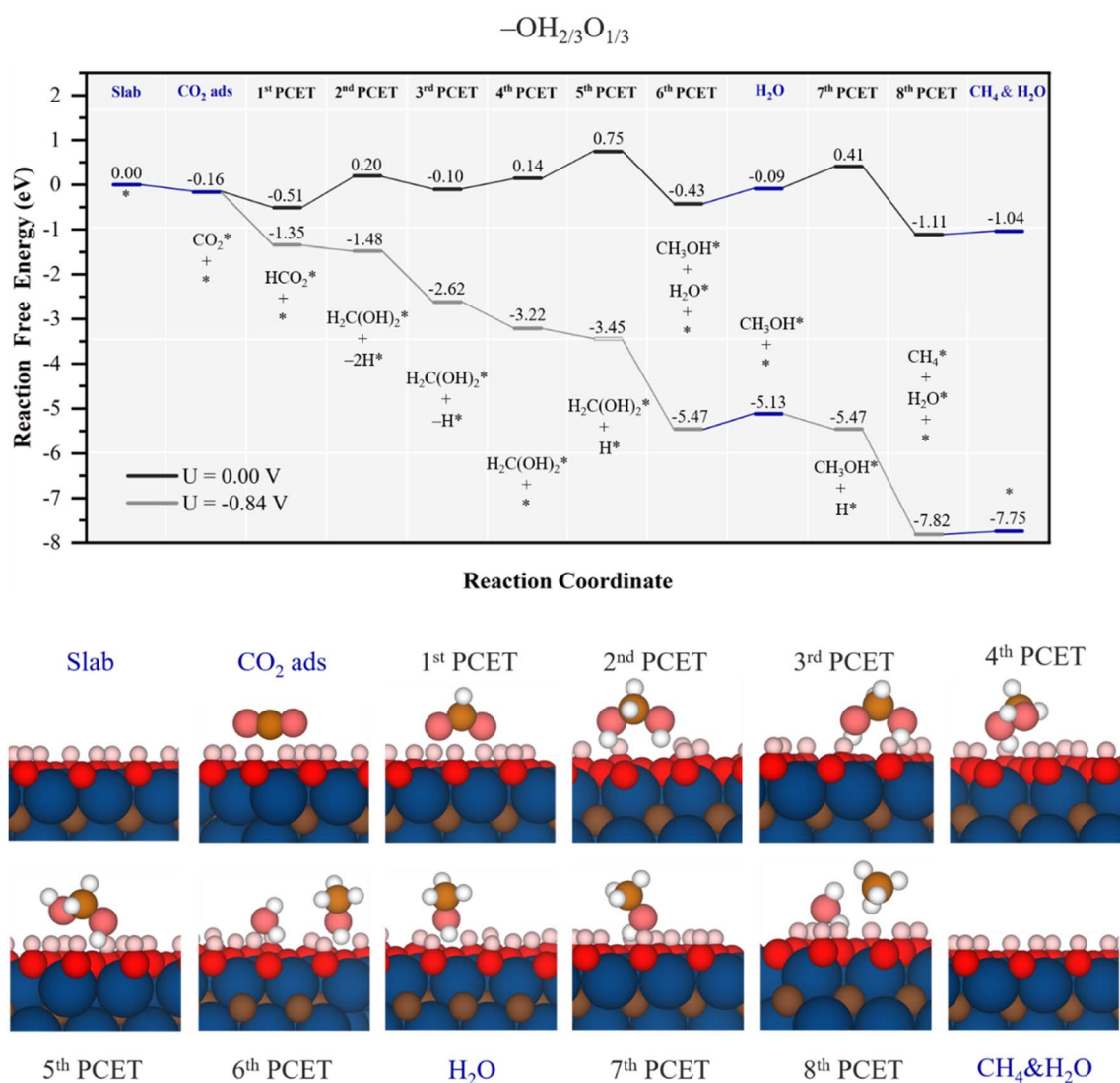

Fig. 6 Gibbs free energy, ΔG, diagram of the CO_2RR on the $-OH_{2/3}O_{1/3}$ Ti$_3$C$_2$ MXene model, under standard working conditions and at a $U = U_L$ calculated potential of -0.84 V *vs.* SHE. Colour code as in Fig. 6. The $nH*$ symbols refer to how many H atoms have been reduced over surface $-O$ groups at the given reaction stage. Bottom panels show side views of atomic structures of different reaction stages. Colour coding as in Fig. 2.
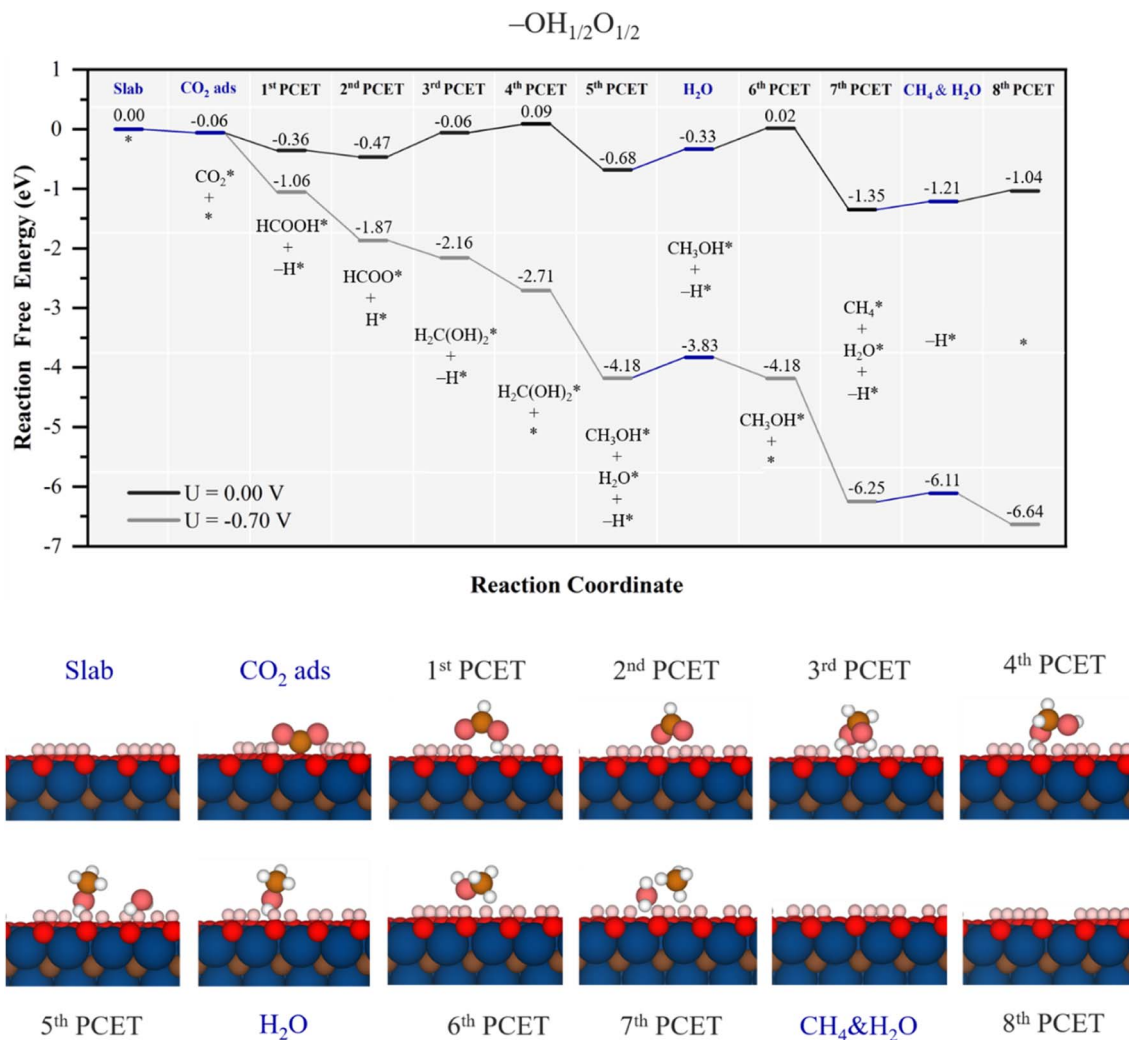
This journal is © The Royal Society of Chemistry 2024

J. Mater. Chem. A, 2024, **12**, 7856–7874 | **7865**

$-OH_{1/2}O_{1/2}$

Fig. 7 Gibbs free energy, ΔG, diagram of the CO_2RR on the $-OH_{1/2}O_{1/2}$ Ti_3C_2 MXene model, under standard working conditions and at a $U = U_L$ calculated potential of -0.70 V vs. SHE. Colour code and notation as in Fig. 6 and 7. Bottom panels show side views of atomic structures of different reaction stages. Colour coding as in Fig. 2.

desorbing, ΔG of 0.63 eV, or refreshing the nearby lost $-OH$ group, $\Delta G = 0.35$ eV, as shown in Fig. S9 of the ESI.† From this point on, again, methanol decomposition into CH_4^* and H_2O^*, implying the joint hydrogenation from a reduced proton and one H from an $-OH$ group, results in an exergonic step with $\Delta G = -1.37$ eV, see Fig. 7, followed by product release and surface regeneration with a ΔG of 0.31 eV. Altogether, the PDS is the electrochemical step leading to adsorbed methanol, ready for its reaction towards CH_4, with a U_L of -0.7 V vs. SHE. This potential would lead also to full $-OH$ termination under strongly acidic conditions, see Fig. S2 of the ESI.†

In any case, the CO_2RR mechanism is essentially kept, with a role of $-O$ surface groups as reducing sites for protons, and later $-OH$ groups as being H-donors, with the steps of formation and decomposition of methylene glycol and methanol, yet here with an initial formation and stabilization of formic acid triggered by the increase of surface $-O$ groups. As per the selectivity, no path to CO is found, while formic acid release is prevented by the high desorption energy of 1.08 eV. Here, the formaldehyde

path implies going through methylene glycol, whose conversion towards methanol is very exergonic by -0.77 eV, and the same applies to methanol decomposition to CH_4. Thus, a high selectivity towards CH_4 would be forecasted, although still the model would compete with the HER, with a U_L of -0.23 V,[53] $H_2^{(g)}$ being the main expected product.

When even increasing the surface $-O$ content, such as in the $-OH_{1/3}O_{2/3}$ model, the reaction path mimics to some extent that of the $-OH_{1/2}O_{1/2}$ model, as shown in Fig. 8 and S10 of the ESI.† Starting from a mild physisorption of CO_2, the first PCET already combines proton reduction with H transfer from $-OH$, forming $HCOOH^*$, with a ΔG value of 0.37 eV. From this point on, the 2nd and 3rd PCETs are essentially isoenergetic proton reductions on surface $-O$ moieties, with the possibility of desorbing HCOOH, requiring 0.4 eV energy, and no more involvement of $-OH$ groups, which may be related to the increase of $E_{H_{vac}}$ up to 0.73 eV, making the H transfer from vicinal $-OH$ groups more difficult. In the 4th PCET, the methylene glycol formation path is essentially isoenergetic by 0.03 eV,
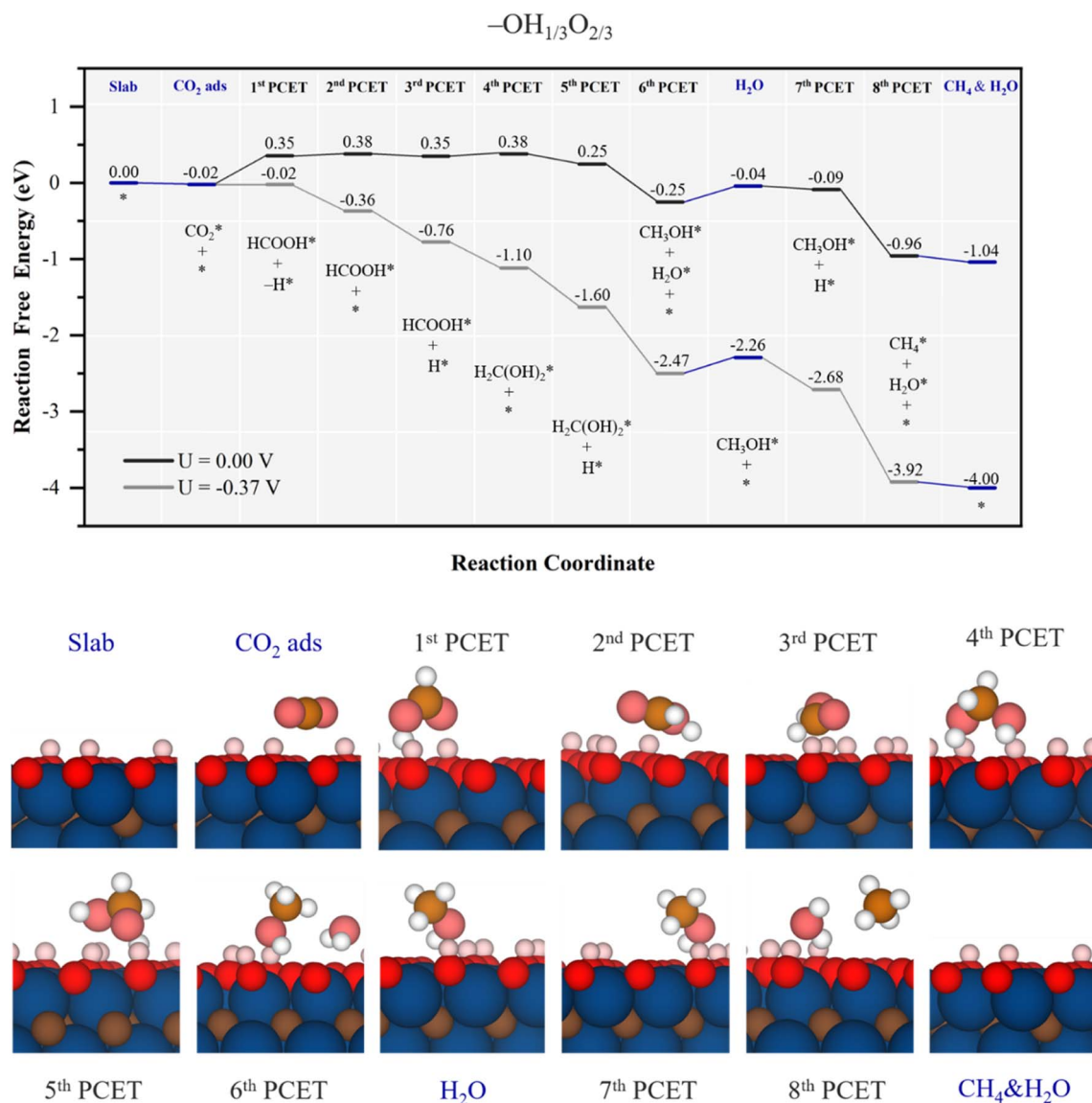
7866 | J. Mater. Chem. A, 2024, **12**, 7856–7874

This journal is © The Royal Society of Chemistry 2024

Fig. 8 Gibbs free energy, ΔG, diagram of the CO_2RR on the $-OH_{1/3}O_{2/3}$ Ti_3C_2 MXene model, under standard working conditions and at a $U = U_L$ calculated potential of -0.37 V vs. SHE. Colour code and notation as in Fig. 6 and 7. Bottom panels show side views of atomic structures of different reaction stages. Colour coding as in Fig. 2.

while CO formation induced by nearby –O proton reduction upon is uphill by 0.36 eV. After this point, the reaction is downhill, first by a –O proton reduction, followed later by methylene glycol decomposition into methanol, with a ΔG of -0.5 eV.

Also similar to the case of the $-OH_{1/2}O_{1/2}$ model, the formed H_2O in methanol synthesis can easily desorb, requiring 0.21 eV, see Fig. 8, while methanol desorption is more costly as it requires 0.51 eV, see Fig. S10 of the ESI.† Actually, the minimum energy path implies proton reduction nearby on an –O site, from which the proton reduction can again be coupled with –OH H transfer, turning the electrochemical step being quite exergonic by -0.87 eV, see Fig. 8. In general terms, the reaction profile is closer to the $\Delta G = 0$ eV than the other inspected models so far, and with less ups and downs in energy, which

translates into reduced limiting potential. In fact, the full process can be made exergonic with a limiting potential of -0.37 V vs. SHE, corresponding to the initial formic acid formation in the first PCET, at variance with previous models, where the PDS is found at a late stage. Still, the U_L is too large for this surface stability, see the Pourbaix diagram in Fig. S2 of the ESI,† and the model would be valid for less acid conditions. Still, as low as the U_L of -0.37 V may seem, as per the selectivity, the $-OH_{1/3}O_{2/3}$ model has a very low U_L for the HER, of solely -0.01 V,[53] and so, the selectivity towards $CH_4^{(g)}$ would be low, and other reaction products, such as HCOOH, CH_3OH, and CO, would be possible with a U_L of -0.37 V, even if their detachment from the surface would be energetically more costly than further reacting towards CH_4, implying a lower content of them.

This journal is © The Royal Society of Chemistry 2024

J. Mater. Chem. A, 2024, **12**, 7856–7874 | **7867**

From the above analysis, one could draw a general trend: namely, the U_L decreases as the –OH proportion decreases. However, no minimum would be expected at a full –O termination. Firstly, according to a previous study conducted by Handoko et al.,[40] a larger U_L of 0.52 V vs. RHE was found for Ti_2CO_2, while Morales et al.[104] pointed out a similar activity between Ti_3C_2 and Ti_2C MXenes. Moreover, according to the Pourbaix diagrams in Fig. S2 of the ESI,† even at zero potential, a full –O termination would require a pH larger than 7, and, as aforementioned, alkaline media is not the best case scenario for the CO_2RR electrocatalytic activity.

At this point, one may wonder what would be the effect of –F surface groups on CO_2RR performance, particularly relevant at low pH and U, see Fig. S2 of the ESI.† This is analysed on the –$F_{1/3}OH_{1/3}O_{1/3}$ model shown in Fig. 9. Actually, if one would assume –F surface groups being mere spectators, the –OH/–O ratio would be comparable to that of the –$OH_{1/2}O_{1/2}$ model, and so a similar performance would be expected, at least in U_L, even if the production rates per electrocatalyst gram would decrease as a third of the surface sites are blocked by –F groups. Mechanistically, as the $E_{H_{vac}}$ value of 0.31 eV is similar to the value of 0.26 eV for the –$OH_{1/2}O_{1/2}$ model, see Table 1, one would envisage a similar involvement of –OH/–O groups in the hydrogenation sequence. By inspecting the actual Gibbs free energy profile in Fig. 9, one observes a small physisorption of CO_2 with an E_{ads} of 0.04 eV, followed by the 1st PCET and nearby –OH H transfer to form HCOOH*, with a $\Delta G = -0.13$ eV, actually reminiscent of that found for the –$OH_{1/2}O_{1/2}$ model. However, on –$F_{1/3}OH_{1/3}O_{1/3}$ the second PCET does not lead to formate, but rather to a regeneration of the consumed –OH, here costly by 0.51 eV, again similar to that corresponding to the –$OH_{1/2}O_{1/2}$ model, with $\Delta G = 0.5$ eV,

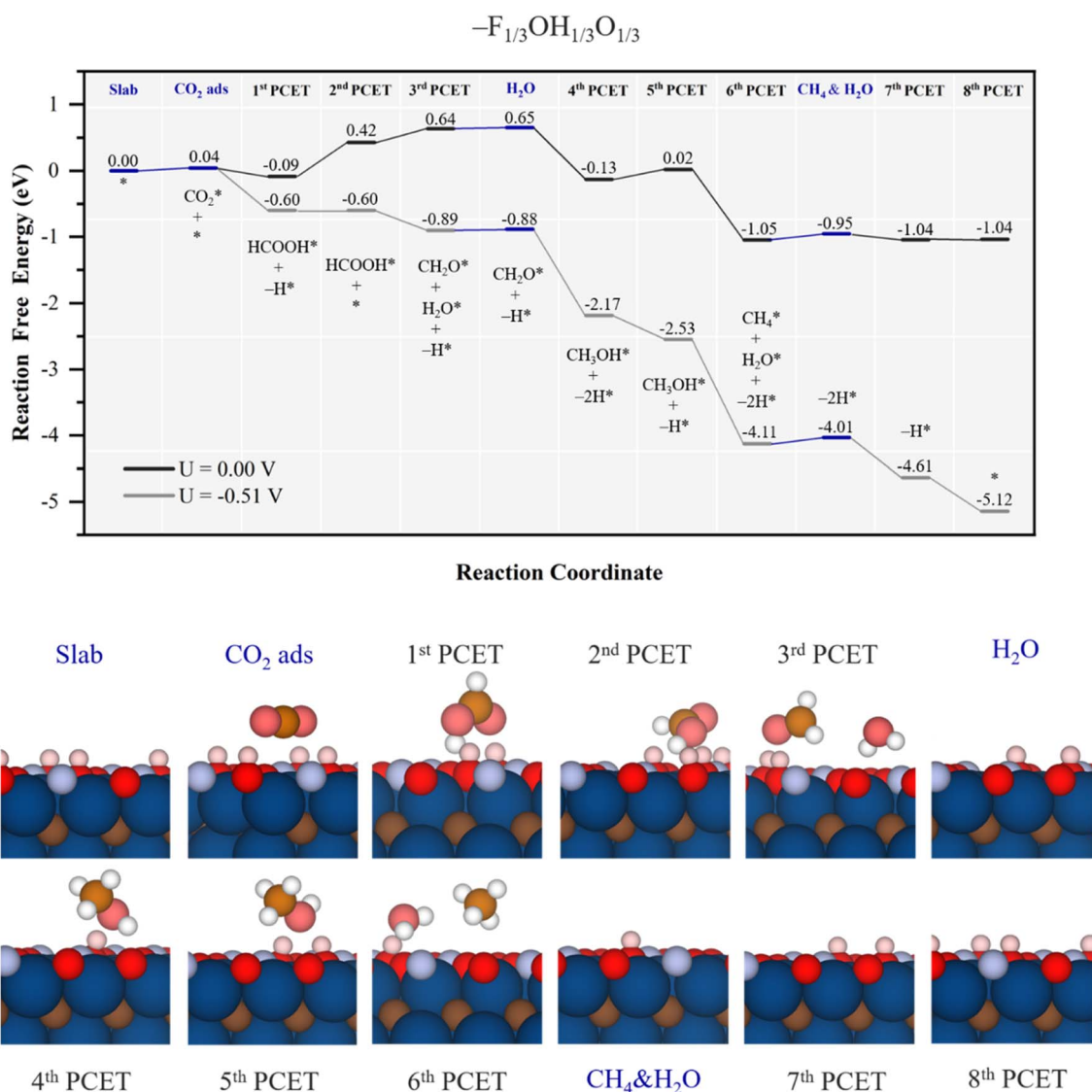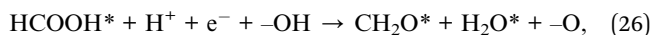Fig. 9 Gibbs free energy, ΔG, diagram of the CO_2RR on the –$F_{1/3}OH_{1/3}O_{1/3}$ Ti_3C_2 MXene model, under standard working conditions and at a $U = U_L$ calculated potential of –0.51 V vs. SHE. Colour code and notation as in Fig. 6 and 7. Bottom panels show side views of atomic structures of different reaction stages. Colour coding as in Fig. 2.

7868 | J. Mater. Chem. A, 2024, 12, 7856–7874

This journal is © The Royal Society of Chemistry 2024

see Fig. 7, and competing with methylene glycol formation, 0.08 eV more costly, see Fig. S11 of the ESI.†

Actually, the absence of the formate intermediate has consequences on the oncoming steps since, at variance with the mechanism for the $-OH_{1/2}O_{1/2}$ model, methylene glycol intermediate formation is not preferred, but the hydrogenation of formic acid coupled with a surface $-OH$ H transfer leads to formaldehyde and water formation, as:

$$HCOOH^* + H^+ + e^- + -OH \rightarrow CH_2O^* + H_2O^* + -O, \quad (26)$$

with a mere cost of 0.22 eV, and preferred over $-O$ reduction by 0.12 eV, and over $HCOOH_{(l)}$ formation, requiring 0.38 eV, see Fig. S11 of the ESI.† Actually, after H_2O^* removal, essentially costless by 0.01 eV, the $CH_2O^{(g)}$ release, costly only by 0.07 eV, competes though with a quite exergonic 4th PCET leading to methanol, again combining one PCTE with one $-OH$ H transfer, with a ΔG of -0.78 eV, see Fig. 9 and S11 of the ESI.† After CH_3OH^* is formed, a vicinal $-OH$ can be easily regenerated by requiring 0.15 eV, and after this Volmer step, methanol can decompose into CH_4^* and H_2O^* coupling H^+ reduction with one H transfer from $-OH$, with a ΔG of -1.07 eV, a process quite competing with the $CH_3OH_{(l)}$ release, requiring 0.44 eV, see Fig. S11 of the ESI.† Once methanol is formed, the 7th and 8th PCETs are used in regenerating two surface $-OH$ groups, with ΔG below 0.01 eV.

Thus, the PDS corresponds to an early step of $-OH$ regeneration right after formic acid formation, with $U_L = -0.51$ V, different from the $-OH$ regeneration right after methanol formation on the $-OH_{1/2}O_{1/2}$ model, with $U_L = -0.70$ V. Actually, the easier reduction cost on $-O$ groups vicinal to CH_3OH^* is the reason behind the change in the reaction profile, lowering the cost of the equivalent PDS on the $-OH_{1/2}O_{1/2}$ model, and leaving the PDS to formic acid formation, essentially unaltered by the presence of $-F$ groups. Thus, on the $-F_{1/3}OH_{1/3}O_{1/3}$ model, the U_L is -0.51 V, close to its stability region according to Pourbaix diagrams, see Fig. S2 of the ESI.† As per the selectivity, formic acid is likely formed under the same U_L, although $CH_2O^{(g)}$ and $CH_3OH_{(l)}$ desorption compete with quite exergonic further reaction steps, moving towards more generation of methane. No channel to CO formation is found, as well. However, as happened with the $-OH_{2/3}O_{1/3}$ model, the main competition is with the HER, with a U_L of solely -0.01 V.[53]

Table 1 summarizes results for the five studied models indicating which PCET is the PDS and to which electrochemical step does it correspond to, including $E_{H_{vac}}$ and U_L values as well. As encompassed in Table 1, but also visible in the captured trends in Fig. 10, the $E_{H_{vac}}$ linearly varies with respect to the $-OH/-O$ ratio, with similar values for the $-OH_{1/2}O_{1/2}$ and $-F_{1/3}OH_{1/3}O_{1/3}$ models. As $E_{H_{vac}}$ increases with the presence of more surface $-O$ groups, the U_L decreases, see Fig. 10, to the point that two regions can be differentiated: one where $-OH$ is the main surface termination site, with quite low U_L values, and the other with the participation of $-O$ groups in reducing protons, and later transferring such H atoms, with even smaller U_L values. The higher involvement of $-O$ surface moieties generally eases the latest PCET steps and moves PDS to an

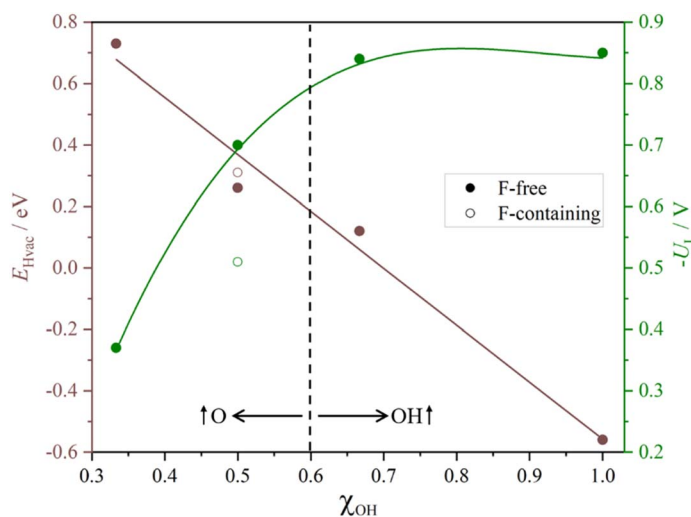**Fig. 10** Plots of H-vacancy energies, $E_{H_{vac}}$, given in eV, and minus the limiting potential, U_L, given in V, as a function of $-OH$ group partition coefficients (χ_{OH}) with respect to $-O$ groups.

earlier stage of the reaction. Last but not least, the presence of $-F$ groups is not *per se* detrimental, and in fact leads to a deviation of the trend, reducing U_L costs. Besides, the reaction profiles question the conventional mechanism of the sole H^+ reduction upon the reacting molecule, and unfolds (i) the sequences of Volmer steps on nearby $-O$ surface groups, followed by H transfer to the reacting molecule from such as-formed $-OH$, (ii) the H transfer from already existing $-OH$ groups, followed by proton reduction on the as-generated $-O$ moieties, and (iii) the simultaneous hydrogenation of a moiety, coupling H^+ reduction electrochemical step with H chemical transfers from surface $-OH$ groups. Indeed, it can be claimed that the simultaneous existence of $-OH$ and $-O$ groups offers a versatility of reactive paths that ultimately expresses in a reduction of the reaction bias cost.

3.3. CO_2RR electrocatalysis performance

We now focus on the CO_2RR performance of the scrutinized models keeping in mind that an optimal catalyst would feature the smallest possible U_L and that the closer the U_L to zero, the higher the activity and faster the CO_2RR kinetics. The present results are already fully consistent with previous studies,[39] in that a higher proportion of $-O$ termination leads to a quite small U_L resulting in a higher CO_2RR activity, see Table 1. However, keeping in mind the electrocatalyst surface stability predicted in the Pourbaix diagram of Fig. S2 of the ESI,† even if certain models feature reduced U_L values, *e.g.* -0.37 V for $-OH_{1/3}O_{2/3}$ or -0.51 V for $-F_{1/3}OH_{1/3}O_{1/3}$, their range of stability implies that at low pH the surface would eventually transform into the full $-OH$ model, or when working at higher pH would imply sluggish reaction conditions, yet to be partially compensated by a larger potential applicability. In addition, the fact that models with larger $-F$ content do not appear in the Pourbaix diagrams helps explaining previous experimental findings,[105] particularly in that such models would make the

This journal is © The Royal Society of Chemistry 2024

J. Mater. Chem. A, 2024, **12**, 7856–7874 | **7869**

reaction infeasible. However, low contents such as is $-F_{1/3}OH_{1/3}O_{1/3}$ are non-detrimental *per se*, as such moieties can help in moving the PDS to an earlier stage, with a concomitant U_L reduction and, hence, operating costs. This opens the door to a control of the electrocatalyst performance by the degree of $-F$ appearing at the surface, a point missed under F-free synthesis methodologies.[73]

Another key point of interest is the comparison of the here reported CO_2RR activity with that of other MXenes reported in the literature, such as fully OH-terminated $Mo_3C_2(OH)_2$,[39] and $Sc_2C(OH)_2$,[41] O-terminated $Mo_3C_2O_2$,[39] Zr_2NO_2,[69] $Ti_3C_2O_2$,[106] and W_2CO_2,[40] pristine surface MXene Mo_2TiC_2,[68] $Mo_2CO_2\text{-}O_v$ model containing surface oxygen vacancies,[107] and $Cr@Nb_2NO_2$,[108] a case with a Cr single atom on a fully $-O$ terminated Nb_2N MXene. No pure $-F$ termination is here compared to, as shown to consistently deliver high U_L for the CO_2RR and HER on MXenes,[42,53] plus is not a reachable stable situation according to Pourbaix diagrams in Fig. S2 of the ESI.† For a more comprehensive comparison, Cu metal is also considered as it has been reported to be a highly efficient CO_2RR catalyst.[41,109] Fig. 11 clearly shows that, even if accounting from deviations from different computational approaches between present models and results in the literature, in general terms, MXene-based electrocatalysts feature lower U_L compared to the Cu reference of -0.93 V, underscoring the potential of such a family of materials for CO_2 conversion purposes. Still, one has to be critical with the display of values. For instance, some of the systems with the lowest U_L are $Mo_2CO_2\text{-}O_v$ and W_2CO_2, with values of -0.31 and -0.35 V, respectively, while to a lower extent, other O-terminated MXenes have relatively low U_L values, like -0.45 V for Zr_2NO_2, -1.04 V for $Ti_3C_2O_2$,[106] or the value of -0.47 V for $Cr@Nb_2NO_2$. However, from the Pourbaix diagram in Fig. S2 of the ESI,† and others reported in the literature, the full O-termination is only stable at positive U_L values, and so, such surface termination gets unrealistic under CO_2RR conditions. Actually, under these conditions, more

realistic values are -1.17 and -0.53 V reported for $Mo_3C_2(OH)_2$ and $Sc_2(OH)_2$, respectively, the latter representing a clear improvement with respect to the Cu reference by around 0.4 V. It is with respect to these fully OH-terminated models where we find that O-rich $-OH_{1/3}O_{2/3}$ and F-containing $-F_{1/3}OH_{1/3}O_{1/3}$ models have an U_L improvement by at least 0.16 and 0.02 V compared with $Sc_2(OH)_2$, underscoring that the slight presence of $-F$ moieties and a balance between $-OH$ and $-O$ groups represent tuning points towards decreasing U_L costs.

In order to understand the differences with prior calculations, one has to note that they are regularly focused on pure $-O$ termination. Thus, the main discrepancy is attributed to the commented involvement of $-F$ and $-OH$ groups, and to the strong hydrophilicity of $-O$ groups. Based on $E_{H_{vac}}$, the strength of this H bond seems to be related to the distribution of $-OH$ groups, which, eventually, endows the MXene surface with a new source of H atoms, making the reaction easier, a feature absent in previous studies with only $-O$ groups. Besides, $-F$ and $-OH$ terminations have the same charge close to $-1e$, but as in the CDD plot in Fig. S5 of the SI,† the electron density on $-F$ termination is more localized, leading to a stronger effective charge, and so, *a priori* more repulsion, features that may affect the MXene activity at different stages of the reaction.

Last but not least, it is worth addressing the competition between the CO_2RR, here examined with respect to methane formation, and the HER, a crucial concurrent reaction in aqueous solutions.[53,110] Even if a rigorous study of the selectivity requires addressing the kinetic barriers,[41,111] the U_L difference among both types of reactions can be used as a sound thermodynamic metric.[112] This is graphically shown in Fig. 12 as a parity plot, gaining HER values from an equivalent previous study.[53] Note that, different from previous studies focusing only on $-O$ terminations,[113,114] we considered here the involvement of
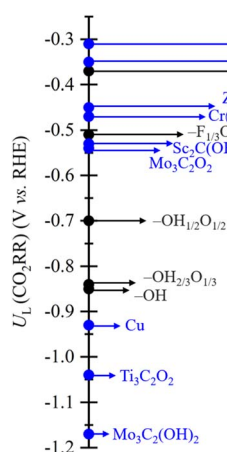

Fig. 11 Comparison of methane U_L from the presently studied terminated models on $Ti_3C_2T_x$ (black dots) along with other values reported in the literature for MXene-based systems, and Cu as a reference (blue dots). All values are given in V.
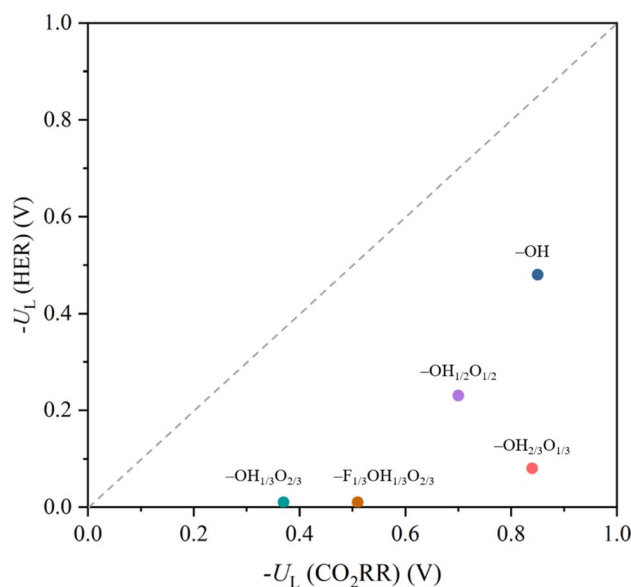

Fig. 12 Comparison of $-U_L$ for the CO_2RR *vs.* $-U_L$ for the HER on the explored terminated $Ti_3C_2T_x$ models. Values for the HER are taken from the literature.[53]

7870 | *J. Mater. Chem. A*, 2024, **12**, 7856–7874

This journal is © The Royal Society of Chemistry 2024

H atoms of the –OH groups, and, in the case of the HER, different reaction mechanisms have been evaluated, beyond the spreadly used, yet limitedly justified, assumption of the reaction being controlled by the first PCET;[108,115] see more details in the literature.[53] Notice that, even if none of the proposed surface terminations is more selective towards the CO_2RR than towards the HER, a general trend can be captured; the smaller the U_L needed, the less the selectivity towards the CO_2RR is. Actually, the CO_2RR selectivity seems to be improved when increasing the –OH/–O ratio, with a maximum for the fully –OH terminated model. Still, even if such models are *per se* selective towards the HER, or very selective, in the cases of the $–OH_{1/3}O_{2/3}$ and $–F_{1/3}OH_{1/3}O_{1/3}$ models, strategies are available to inhibit the HER, such as limiting H^+ transfer rates,[116–118] employing non-water proton donors,[119,120] limiting electron transfer rates,[121,122] or regulating the magnetic moment of the active site.[123]

4. Conclusions

Here we have profoundly analyzed the possible use of Ti_3C_2 MXene based materials as electrocatalysts for the CO_2RR, examining the surface composition under working conditions *via* Pourbaix diagrams and systematically studying the reaction mechanisms considering the involvement of different surface termination species, and aspects such as limiting potential towards methane production, selectivity, and competition with respect to $H_2^{(g)}$ production. Based on the surface stability dictated by the calculated Pourbaix diagrams, several surface models are investigated that may have potential interest towards the CO_2RR, namely full –OH, as well as $–OH_{2/3}O_{1/3}$, $–OH_{1/2}O_{1/2}$, and $–OH_{1/3}O_{2/3}$ models, and the F-containing $–F_{1/3}OH_{1/3}O_{1/3}$ model. Apart from their stability under working conditions, kinetic phase diagrams show that these models meet the requirement of CO_2 capture and activation, and the CH_4 product release.

The calculated reaction Gibbs free energy profiles reveal that, in general, for F-free models the reaction mechanism involves formic acid and methylene glycol formation, which decomposes into methanol and water. In subsequent steps, methanol decomposes into methane and water as well. However, on the F-containing $–F_{1/3}OH_{1/3}O_{1/3}$ model, the reaction involves the initial formation of formic acid, and its decomposition into formaldehyde, which later hydrogenates up to methanol. The present profiles help in understanding the experimental observations, in the sense that, the larger the –O content, the smaller the U_L,[42] mostly arising from the dual role of –O and –OH groups, acting as H acceptors and donors, respectively, which make the hydrogenation steps more flexible, allowing for reduction of U_L costs, and also add the possibility of reaction species to be simultaneously hydrogenated from H^+ reduction and surface –OH group H transfers, the latest fostered by a relatively low energetic cost of deprotonation. Note that the role of the –OH groups is reminiscent of the Mars-van Krevelen mechanism on oxide surfaces where the lattice O directly participates in the reaction with the left O vacancy healed by O_2 from the gas phase at a subsequent step.

Generally speaking, the presently studied $Ti_3C_2T_x$ surface MXene models, together with results from the literature, underscore the effectiveness of such materials for the CO_2RR when compared to the reference Cu electrocatalyst, with significantly improved U_L values by up to *ca.* 0.6 V. However, they still face aspects to be improved; on one hand, the required U_L in many of the models with binary and ternary terminations underscores the eventual gradual conversion into a fully –OH terminated model, which has a larger value of U_L of −0.85 V, yet lower by almost 0.1 V than the equivalent value for the Cu reference. On the other hand, the selectivity of the CO_2RR on the studied models with respect to the HER is far from optimal, yet the fully –OH terminated model is the most competitive one, and so significant degrees of the CO_2RR are to be expected when using it for this purpose. In any case, on such surface terminated $Ti_3C_2T_x$ MXenes, an optimal HER performance is to be expected at low U_L values, while a significant improvement in the CO_2RR is to be expected when reducing the U_L up to the requirements of the fully –OH terminated model. Given the vast family of possible MXene materials, and the surface tunability, the present study sheds light on the effective selection and tuning of MXenes for high performance and selective CO_2RR electrocatalysis.

Conflicts of interest

There are no conflicts of interest to declare.

Acknowledgements

References

1 *International Energy Agency: CO₂ Emissions In 2022; Typeset in France by IEA - March 2023*, **https://www.iea.org/**.

2 *European Central Bank: Looking Through Higher Energy Prices? Monetary Policy and The Preen Transition*, **https:// www.ecb.europa.eu/home/html/index.en.html**.

3 S. Posada-Pérez, F. Viñes, P. J. Ramirez, A. B. Vidal, J. A. Rodriguez and F. Illas, *Phys. Chem. Chem. Phys.*, 2014, **16**, 14912–14921.

This journal is © The Royal Society of Chemistry 2024

J. Mater. Chem. A, 2024, **12**, 7856–7874 | **7871**

4 X. Liu, C. Kunkel, P. Ramírez de la Piscina, N. Homs, F. Viñes and F. Illas, *ACS Catal.*, 2017, **7**, 4323–4335.

5 J. A. Rodriguez, J. Evans, L. Feria, A. B. Vidal, P. Liu, K. Nakamura and F. Illas, *J. Catal.*, 2013, **307**, 162–169.

6 G. Pacchioni, J. M. Ricart and F. Illas, *J. Am. Chem. Soc.*, 1994, **116**, 10152–10158.

7 S. Posada-Pérez, P. J. Ramírez, J. Evans, F. Viñes, P. Liu, F. Illas and J. A. Rodriguez, *J. Am. Chem. Soc.*, 2016, **138**, 8269–8278.

8 S. Yang, M. Jiang, W. Zhang, Y. Hu, J. Liang, Y. Wang, Z. Tie and Z. Jin, *Adv. Funct. Mater.*, 2023, **33**, 2301984.

9 C. Sun, Y. Hou, N. Lüdi, H. Hu, M. de Jesús Gálvez-Vázquez, M. Liechti, Y. Kong, M. Liu, R. Erni, A. V. Rudnev and P. Broekmann, *J. Catal.*, 2022, **407**, 198–205.

10 M. Liu, Y. Pang, B. Zhang, P. De Luna, O. Voznyy, J. Xu, X. Zheng, C. T. Dinh, F. Fan, C. Cao, F. P. G. Arquer, T. S. Safaei, A. Mepham, A. Klinkova, E. Kumacheva, T. Filleter, D. Sinton, S. O. Kelley and E. H. Sargent, *Nature*, 2016, **537**, 382–386.

11 M. J. Cheng, E. L. Clark, H. H. Pham, A. T. Bell and M. Head-Gordon, *ACS Catal.*, 2016, **6**, 7769–7777.

12 K. P. Kuhl, T. Hatsukade, E. R. Cave, D. N. Abram, J. Kibsgaard and T. F. Jaramillo, *J. Am. Chem. Soc.*, 2014, **136**, 14107–14113.

13 Y. Chen, J. Zhang, L. Yang, X. Wang, Q. Wu and Z. Hu, *Electrochem. Energy Rev.*, 2022, **5**, 11.

14 J. J. Wang, X. P. Li, B. F. Cui, Z. Zhang, X. F. Hu, J. Ding, Y. D. Deng, X. P. Han and W. B. Hu, *Rare Met.*, 2021, **40**, 3019–3037.

15 H. Hu, J. Z. Ou, X. Xu, Y. Lin, Y. Zhang, H. Zhao, D. Chen, M. He, Y. Huang and L. Deng, *J. Chem. Eng.*, 2021, **425**, 130587.

16 S. Zhou, W. Pei, Y. Zhao, X. Yang, N. Liu and J. Zhao, *Npj Comput. mater.*, 2021, **7**, 186.

17 K. P. Kuhl, E. R. Cave, D. N. Abram and T. F. Jaramillo, *Energy Environ. Sci.*, 2012, **5**, 7050–7059.

18 D. Ren, Y. Deng, A. D. Handoko, C. S. Chen, S. Malkhandi and B. S. Yeo, *ACS Catal.*, 2015, **5**, 2814–2821.

19 Y. Hori, A. Murata and R. Takahashi, *J. Chem. Soc., Faraday Trans.*, 1989, **85**, 2309–2326.

20 Y. Huang, A. D. Handoko, P. Hirunsit and B. S. Yeo, *ACS Catal.*, 2017, **7**, 1749–1756.

21 H. Shin, Y. Ha and H. Kim, *J. Phys. Chem.*, 2016, **7**, 4124–4129.

22 X. Liu, J. Xiao, H. Peng, X. Hong, K. Chan and J. K. Nørskov, *Nat. Commun.*, 2017, **8**, 15438.

23 Á. Morales-García, F. Calle-Vallejo and F. Illas, *ACS Catal.*, 2020, **10**, 13487–13503.

24 M. Naguib, J. Halim, J. Lu, K. M. Cook, L. Hultman, Y. Gogotsi and M. W. Barsoum, *J. Am. Chem. Soc.*, 2013, **135**, 15966–15969.

25 M. Naguib, V. Presser, N. Lane, D. Tallman, Y. Gogotsi, J. Lu, L. Hultman and M. W. Barsoum, *RSC Adv.*, 2011, **1**, 1493–1499.

26 M. Ahmaruzzaman, *RSC Adv.*, 2022, **12**, 34766–34789.

27 G. Deysher, C. E. Shuck, K. Hantanasirisakul, N. C. Frey, A. C. Foucher, K. Maleski, A. Sarycheva, V. B. Shenoy, E. A. Stach, B. Anasori and Y. Gogotsi, *ACS Nano*, 2020, **14**, 204–217.

28 M. Naguib, O. Mashtalir, J. Carle, V. Presser, J. Lu, L. Hultman, Y. Gogotsi and M. W. Barsoum, *ACS Nano*, 2012, **6**, 1322–1331.

29 M. Ghidiu, M. R. Lukatskaya, M.-Q. Zhao, Y. Gogotsi and M. W. Barsoum, *Nature*, 2014, **516**, 78–81.

30 X. Q. Tan, W. Mo, X. Lin, J. Y. Loh, A. R. Mohamed and W. J. Ong, *Nanoscale*, 2023, **15**, 6536–6562.

31 M. A. Hope, A. C. Forse, K. J. Griffith, M. R. Lukatskaya, M. Ghidiu, Y. Gogotsi and C. P. Grey, *Phys. Chem. Chem. Phys.*, 2016, **18**, 5099–5102.

32 B. C. Wyatt, A. Rosenkranz and B. Anasori, *Adv. Mater.*, 2021, **33**, 2007973.

33 M. Benchakar, L. Loupias, C. Garnero, T. Bilyk, C. Morais, C. Canaff, N. Guignard, S. Morisset, H. Pazniak, S. Hurand, P. Chartier, J. Pacaud, V. Mauchamp, M. W. Barsoum, A. Habrioux and S. Célérier, *Appl. Surf. Sci.*, 2020, **530**, 147209.

34 J. Sun, B. Liu, Q. Zhao, C. H. Kirk and J. Wang, *Adv. Mater.*, 2023, **35**, 2306072.

35 S. Y. Pang, Y. T. Wong, S. Yuan, Y. Liu, M. K. Tsang, Z. Yang, H. Huang, W. T. Wong and J. Hao, *J. Am. Chem. Soc.*, 2019, **141**, 9610–9616.

36 R. Meshkian, H. Lind, J. Halim, A. El Ghazaly, J. Thörnberg, Q. Tao, M. Dahlqvist, J. Palisaitis, P. O. Å. Persson and J. Rosen, *ACS Appl. Nano Mater.*, 2019, **2**, 6209–6219.

37 V. Kamysbayev, A. S. Filatov, H. Hu, X. Rui, F. Lagunas, D. Wang, R. F. Klie and D. V. Talapin, *Science*, 2020, **369**, 979–983.

38 D. Ontiveros, F. Viñes and C. Sousa, *J. Mater. Chem. A*, 2023, **11**, 13754–13764.

39 N. Li, X. Chen, W. J. Ong, D. R. MacFarlane, X. Zhao, A. K. Cheetham and C. Sun, *ACS Nano*, 2017, **11**, 10825–10833.

40 A. D. Handoko, K. H. Khoo, T. L. Tan, H. Jin and Z. W. Seh, *J. Mater. chem. A*, 2018, **6**, 21885–21890.

41 H. Chen, A. D. Handoko, J. Xiao, X. Feng, Y. Fan, T. Wang, D. Legut, Z. W. Seh and Q. Zhang, *ACS Appl. Mater. Interfaces*, 2019, **11**, 36571–36579.

42 A. D. Handoko, H. Chen, Y. Lum, Q. Zhang, B. Anasori and Z. W. Seh, *iScience*, 2020, **23**, 101181.

43 C. Y. J. Lim, A. D. Handoko and Z. W. Seh, *Diamond Relat. Mater.*, 2022, **130**, 109461.

44 G. T. M. Kadja, M. M. Ilm, N. J. Azhar, A. Febrianti, J. J. M. Siregar, N. Nurdini, U. Pratomo and M. I. Khalil, *FlatChem*, 2023, **38**, 100481.

45 X. Li, Y. Chen, X. Zhan, Y. Xu, L. Hao, L. Xu, X. Li, M. Umer, X. Tan, B. Han, A. W. Robertson and Z. Sun, *Innov. Mater.*, 2023, **1**, 100014.

46 H. Bao, Y. Qiu, X. Peng, J.-a. Wang, Y. Mi, S. Zhao, X. Liu, Y. Liu, R. Cao, L. Zhuo, J. Ren, J. Sun, J. Luo and X. Sun, *Nat. Commun.*, 2021, **12**, 238.

47 Y. Zhang and Z. Cao, *J. Phys. Chem. C*, 2021, **125**, 13331–13342.

48 X. Qian, L. Li, Y. Li, Z. Liu, Z. Tian, C. Zhan and L. Chen, *Phys. Chem. Chem. Phys.*, 2021, **23**, 12431–12438.

7872 | *J. Mater. Chem. A*, 2024, **12**, 7856–7874

This journal is © The Royal Society of Chemistry 2024

49 M. Naguib, M. Kurtoglu, V. Presser, J. Lu, J. Niu, M. Heon, L. Hultman, Y. Gogotsi and M. W. Barsoum, *Adv. Mater.*, 2011, **23**, 4248–4253.

50 M. Tahir, A. Ali Khan, S. Tasleem, R. Mansoor and W. K. Fan, *Energy Fuels*, 2021, **35**, 10374–10404.

51 M. Pourbaix, *Atlas of Electrochemical Equilibria in Aqueous Solutions*, National Association of Corrosion Engineers (NACE), Houston, Texas, USA, 1974.

52 M. López, K. S Exner, F. Viñes and F. Illas, *Adv. Theory Simul.*, 2023, **6**, 2200217.

53 L. Meng, L. K. Yan, F. Viñes and F. Illas, *J. Mater. Chem. A*, 2023, **11**, 6886–6900.

54 Y. Cheng, X. Xu, Y. Li, Y. Zhang and Y. Song, *Comput. Mater. Sci.*, 2022, **202**, 110971.

55 X. Qian, L. Li, Y. Li, Z. Liu, Z. Tian, C. Zhan and L. Chen, *Phys. Chem. Chem. Phys.*, 2021, **23**, 12431–12438.

56 G. Kresse and J. Furthmüller, *Phys. Rev. B*, 1996, **54**, 11169–11186.

57 J. P. Perdew, K. Burke and M. Ernzerhof, *Phys. Rev. Lett.*, 1996, **77**, 3865–3868.

58 J. D. Gouveia, Á. Morales-García, F. Viñes, J. R. B. Gomes and F. Illas, *ACS Nano*, 2022, **16**, 12541–12552.

59 V. Parey, B. M. Abraham, S. H. Mir and J. K. Singh, *ACS Appl. Mater. Interfaces*, 2021, **13**, 35585–35594.

60 G. Gao, A. P. O'Mullane and A. Du, *ACS Catal.*, 2017, **7**, 494–500.

61 S. Grimme, J. Antony, S. Ehrlich and H. Krieg, *J. Chem. Phys.*, 2010, **132**, 154104.

62 P. E. Blöchl, *Phys. Rev. B*, 1994, **50**, 17953–17979.

63 G. Kresse and D. Joubert, *Phys. Rev. B*, 1999, **59**, 1758–1775.

64 R. Morales-Salvador, J. D. Gouveia, Á. Morales-García, F. Viñes, J. R. B. Gomes and F. Illas, *ACS Catal.*, 2021, **11**, 11248–11255.

65 K. Mathew, V. S. C. Kolluru, S. Mula, S. N. Steinmann and R. G. Hennig, *J. Chem. Phys.*, 2019, **151**, 234101.

66 H. J. Monkhorst and J. D. Pack, *Phys. Rev. B*, 1976, **13**, 5188–5192.

67 M. López, Á. Morales-García, F. Viñes and F. Illas, *ACS Catal.*, 2021, **11**, 12850–12857.

68 J. D. Gouveia, Á. Morales-García, F. Viñes, F. Illas and J. R. B. Gomes, *Appl. Catal., B*, 2020, **260**, 118191.

69 J. K. Nørskov, J. Rossmeisl, A. Logadottir, L. Lindqvist, J. R. Kitchin, T. Bligaard and H. Jónsson, *J. Phys. Chem. B*, 2004, **108**, 17886–17892.

70 H. A. Hansen, I. C. Man, F. Studt, F. Abild-Pedersen, T. Bligaard and J. Rossmeisl, *Phys. Chem. Chem. Phys.*, 2010, **12**, 283–290.

71 W. Yuan, L. Cheng, Y. An, H. Wu, N. Yao, X. Fan and X. Guo, *ACS Sustain. Chem. Eng.*, 2018, **6**, 8976–8982.

72 N. A. Adibah, S. N. A. Zaine and M. F. A. Shukur, *Mater. Sci. Forum*, 2021, **1023**, 15–20.

73 T. Li, L. Yao, Q. Liu, J. Gu, R. Luo, J. Li, X. Yan, W. Wang, P. Liu, B. Chen, W. Zhang, W. Abbas, R. Naz and D. Zhang, *Angew. Chem., Int. Ed.*, 2018, **57**, 6115–6119.

74 Z. Guo, Y. Li, B. Sa, Y. Fang, J. Lin, Y. Huang, C. Tang, J. Zhou, N. Miao and Z. Sun, *Appl. Surf. Sci.*, 2020, **521**, 146436.

75 Y. Li, Y. Chen, Z. Guo, C. Tang, B. Sa, N. Miao, J. Zhou and Z. Sun, *J. Chem. Eng.*, 2022, **429**, 132171.

76 V. Parey, B. M. Abraham, M. V. Jyothirmai and J. K. Singh, *Catal. Sci. Technol.*, 2022, **12**, 2223–2231.

77 S. Nitopi, E. Bertheussen, S. B. Scott, X. Liu, A. K. Engstfeld, S. Horch, B. Seger, I. E. L. Stephens, K. Chan, C. Hahn, J. K. Nørskov, T. F. Jaramillo and I. Chorkendorff, *Chem. Rev.*, 2019, **119**, 7610–7672.

78 I. Fishtik and R. Datta, *Chem. Eng. Sci.*, 2000, **55**, 4029–4043.

79 Y. Xiao and W. Zhang, *Nanoscale*, 2020, **12**, 7660–7673.

80 J. N. Brønsted, *Chem. Rev.*, 1928, **5**, 231–338.

81 K. Niu, L. Chi, J. Rosen and J. Björk, *J. Phys. Chem. Lett.*, 2022, **13**, 2800–2807.

82 K. S. Exner and H. Over, *Acc. Chem. Res.*, 2017, **50**, 1240–1247.

83 M. López, K. S. Exner, F. Viñes and F. Illas, *J. Catal.*, 2023, **421**, 252–263.

84 H. Chen, A. D. Handoko, T. Wang, J. Qu, J. Xiao, X. Liu, D. Legut, Z. Wei Seh and Q. Zhang, *ChemSusChem*, 2020, **13**, 5690–5698.

85 N. Li, X. Wang, X. Lu, P. Zhang and W. J. Ong, *Chem.–An Euro. J.*, 2021, **27**, 17900–17909.

86 S. Baskaran and J. Jung, *Appl. Surf. Sci.*, 2022, **592**, 153339.

87 *NIST Standard Reference Database SRD Number 69*, DOI: **10.18434/T4D303**.

88 Q. Li, Y. Ouyang, S. Lu, X. Bai, Y. Zhang, L. Shi, C. Ling and J. Wang, *Chem. Commun.*, 2020, **56**, 9937–9949.

89 Á. Morales-García, A. Fernández-Fernández, F. Viñes and F. Illas, *J. Mater. Chem. A*, 2018, **6**, 3381–3385.

90 R. Morales-Salvador, Á. Morales-García, F. Viñes and F. Illas, *Phys. Chem. Chem. Phys.*, 2018, **20**, 17117–17124.

91 *Collision Theory*, Chemistry LibreTexts, Libretexts, 2017.

92 S. Pogodin and N. López, *ACS Catal.*, 2014, **4**, 2328–2332.

93 R. Bisson, M. Sacchi, T. T. Dang, B. Yoder, P. Maroni and R. D. Beck, *J. Phys. Chem. A*, 2007, **111**, 12679–12683.

94 C. Kunkel, F. Viñes and F. Illas, *Energy Environ. Sci.*, 2016, **9**, 141–144.

95 T. Shimanouchi, *Tables of Molecular Vibrational Frequencies Consolidated Volume I*, National Bureau of Standards, 1972, pp. 1–160.

96 P. W. Atkins and J. De Paula, *Atkins' Physical Chemistry*. Oxford University Press, 8th edn, 2006.

97 A. V. Leont'eva, A. Y. Zakharov and A. Y. Prokhorov, *arXiv*, 2017, preprint, arXiv:1708.08077, DOI: **10.48550/arXiv.1708.08077**.

98 H. Ooka, J. Huang and K. S. Exner, *Front. Energy Res.*, 2021, **9**, 654460.

99 J. R. Pankhurst, P. Iyengar, A. Loiudice, M. Mensi and R. Buonsanti, *Chem. Sci.*, 2020, **11**, 9296–9302.

100 A. Mazheika, Y. G. Wang, R. Valero, F. Viñes, F. Illas, L. M. Ghiringhelli, S. V. Levchenko and M. Scheffler, *Nat. Commun.*, 2022, **13**, 419.

101 M. López, L. Broderick, J. J. Carey, F. Viñes, M. Nolan and F. Illas, *Phys. Chem. Chem. Phys.*, 2018, **20**, 22179–22186.

102 H. Prats, H. McAloone, F. Viñes and F. Illas, *J. Mater. Chem. A*, 2020, **8**, 12296–12300.

This journal is © The Royal Society of Chemistry 2024

J. Mater. Chem. A, 2024, **12**, 7856–7874 | **7873**

103 J. D. Wiensch, J. John, J. M. Velazquez, D. A. Torelli, A. P. Pieterick, M. T. McDowell, K. Sun, X. Zhao, B. S. Brunschwig and N. S. Lewis, *ACS Energy Lett.*, 2017, **2**, 2234–2238.

104 Á. Morales-García, M. Mayans-Llorach, F. Viñes and F. Illas, *Phys. Chem. Chem. Phys.*, 2019, **21**, 23136–23142.

105 A. D. Handoko, K. D. Fredrickson, B. Anasori, K. W. Convey, L. R. Johnson, Y. Gogotsi, A. Vojvodic and Z. W. Seh, *ACS Appl. Energy Mater.*, 2018, **1**, 173–180.

106 N. H. Attanayake, H. R. Banjade, A. C. Thenuwara, B. Anasori, Q. Yan and D. R. Strongin, *Chem. Commun.*, 2021, **57**, 1675–1678.

107 S. Cao, Y. Hu, C. Yang, J. Li, H. Chen, S. Wei, S. Liu, Z. Wang, D. Sun and X. Lu, *J. CO$_2$ Util.*, 2022, **62**, 102074.

108 S. Lu, Y. Zhang, F. Lou and Z. Yu, *J. CO$_2$ Util.*, 2022, **62**, 102069.

109 A. A. Peterson, F. Abild-Pedersen, F. Studt, J. Rossmeisl and J. K. Nørskov, *Energy Environ. Sci.*, 2010, **3**, 1311–1315.

110 Z. W. Seh, K. D. Fredrickson, B. Anasori, J. Kibsgaard, A. L. Strickler, M. R. Lukatskaya, Y. Gogotsi, T. F. Jaramillo and A. Vojvodic, *ACS Energy Lett.*, 2016, **1**, 589–594.

111 C. Shi, H. A. Hansen, A. C. Lausche and J. K. Nørskov, *Phys. Chem. Chem. Phys.*, 2014, **16**, 4720–4727.

112 X. Hong, K. Chan, C. Tsai and J. K. Nørskov, *ACS Catal.*, 2016, **6**, 4428–4437.

113 Y. W. Cheng, J. H. Dai, Y. M. Zhang and Y. Song, *J. Mater. Chem. A*, 2018, **6**, 20956–20965.

114 Y. W. Cheng, J.-H. Dai, Y. M. Zhang and Y. Song, *J. Phys. Chem. C*, 2018, **122**, 28113–28122.

115 S. Lu, H. L. Huynh, F. Lou, M. Guo and Z. Yu, *J. CO$_2$ Util.*, 2021, **51**, 101645.

116 B. L. Sheets and G. G. Botte, *ChemComm*, 2018, **54**, 4250–4253.

117 M. A. Ortuño, O. Hollóczki, B. Kirchner and N. López, *J. Phys. Chem. Lett.*, 2019, **10**, 513–517.

118 J. M. McEnaney, A. R. Singh, J. A. Schwalbe, J. Kibsgaard, J. C. Lin, M. Cargnello, T. F. Jaramillo and J. K. Nørskov, *Energy Environ. Sci.*, 2017, **10**, 1621–1630.

119 S. Malkhandi, B. Yang, A. K. Manohar, G. K. S. Prakash and S. R. Narayanan, *J. Am. Chem. Soc.*, 2013, **135**, 347–353.

120 A. K. Manohar, S. Malkhandi, B. Yang, C. Yang, G. K. Surya Prakash and S. R. Narayanan, *J. Electrochem. Soc.*, 2012, **159**, A1209.

121 K. A. Brown, D. F. Harris, M. B. Wilker, A. Rasmussen, N. Khadka, H. Hamby, S. Keable, G. Dukovic, J. W. Peters, L. C. Seefeldt and P. W. King, *Science*, 2016, **352**, 448–450.

122 D. Zhu, L. Zhang, R. E. Ruther and R. J. Hamers, *Nat. Mater.*, 2013, **12**, 836–841.

123 X. Guo and S. Huang, *Electrochim. Acta*, 2018, **284**, 392–399.

7874 | *J. Mater. Chem. A*, 2024, **12**, 7856–7874

This journal is © The Royal Society of Chemistry 2024